Department of Applied Physics

Non-catalytic growth of metal oxide nanowires: properties and growth mechanism investigations

Simas Rackauskas

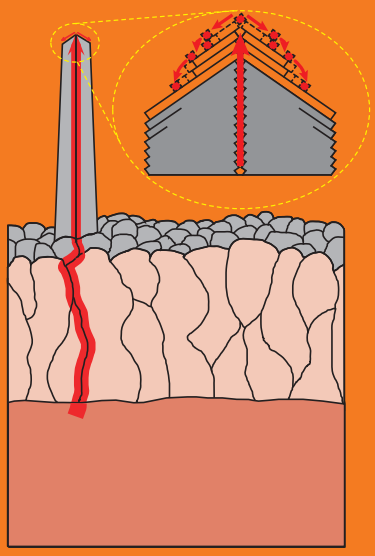

Aalto University

DOCTORAL DISSERTATIONS

Aalto University publication series
DOCTORAL DISSERTATIONS 132/2011

Non-catalytic growth of metal oxide nanowires: properties and growth mechanism investigations

Simas Rackauskas

Doctoral dissertation for the degree of Doctor of Science in Technology/ in Architecture (Doctor of Philosophy) to be presented with due permission of the School of Science for public examination and debate in Auditorium 239 of the Engineering Physics building at the Aalto University School of Science (Otakaari 3, Espoo, Finland) on the 2nd of December 2011 at 12 noon.

Aalto University
School of Science
Department of Applied Physics
NanoMaterials

Supervisor
Prof. Esko I. Kauppinen

Instructor
Dr. Albert G. Nasibulin

Preliminary examiners
Prof. Markku Leskelä, University of Helsinki
Prof. Jorma Jokiniemi, University of Kuopio

Opponent
Dr. Stephan Hofmann, University of Cambridge, UK

Aalto University publication series
DOCTORAL DISSERTATIONS 132/2011

ISBN 978-952-60-4406-4 (pdf)
ISBN 978-952-60-4405-7 (printed)
ISSN-L 1799-4934
ISSN 1799-4942 (pdf)
ISSN 1799-4934 (printed)

Unigrafia Oy
Helsinki 2011

Finland

The dissertation can be read at http://lib.tkk.fi/Diss/

441 697
Printed matter

Aalto University

Abstract

Aalto University, P.O. Box 11000, FI-00076 Aalto www.aalto.fi

Author
Simas Rackauskas

Name of the doctoral dissertation
Non-catalytic growth of metal oxide nanowires: properties and growth mechanism investigations

Publisher School of Science

Unit Department of Applied Physics

Series Aalto University publication series DOCTORAL DISSERTATIONS 132/2011

Field of research Nanomaterials

Manuscript submitted 18 October 2011 **Manuscript revised** 7 November 2011

Date of the defence 2 December 2011 **Language** English

☐ **Monograph** ☒ **Article dissertation (summary + original articles)**

Abstract

This thesis is devoted to the non-catalytic syntheses of metal oxide nanowires (NWs), and investigations of their properties and growth mechanisms. Two different approaches were applied for the syntheses — metal resistive heating and vapor growth methods. The products were thoroughly characterized by electron microscopy, optical and X-ray characterization techniques. The synthesized NWs were examined for field emission (FE) and ultraviolet (UV) sensing applications.

The resistive heating of various metals was demonstrated to be an efficient, simple and rapid method for the synthesis of CuO, Fe_2O_3, V_2O_5 and ZnO NWs under ambient air conditions. Fe_2O_3 NW formation was detected after just 2 s of heating; other metal oxide NWs were grown after 10 s. The NW growth mechanism during metal oxidation was explained based on observations of ZnO and Fe_2O_3 NW growth. The mechanism is based on the diffusion of metal ions to the surface through grain boundaries and to the tip of the growing NW through defect diffusion and by surface diffusion. FE from NWs grown by the resistive heating method exibited promising results for applications in vacuum electronic devices. Cold electron FE measurements showed that CuO NWs have a very low threshold electric field of 4 V/μm at a current density of 0.01 mA/cm^2.

For the vapor growth of ZnO tetrapods (ZnO-Ts) a vertical flow reactor was designed and constructed. It was shown that the morphology of ZnO-Ts could be adjusted via the Zn vapor pressure in the reactor. The highest aspect ratio of ZnO-T legs was obtained at 700 °C, at a Zn partial pressure of 0.08 atm. ZnO-Ts demonstrated application possibilities for transparent and flexible UV sensors. Sensors based on ZnO-Ts showed a 45-fold current increase under UV irradiation with an intensity of 30 μW/cm^2 at a wavelength of 365 nm, and a response time of 0.9 s. The high performance of the device was explained by the multiple contact barriers.

Keywords Metal oxide nanowires, non-catalytic, synthesis, growth mechanism, field emission, UV sensing

ISBN (printed) 978-952-60-4405-7 **ISBN (pdf)** 978-952-60-4406-4

ISSN-L 1799-4934 **ISSN (printed)** 1799-4934 **ISSN (pdf)** 1799-4942

Location of publisher Espoo **Location of printing** Helsinki **Year** 2011

Pages 103 **The dissertation can be read at** http://lib.tkk.fi/Diss/

Preface

The research work for the present thesis was carried out in the Nanomaterials Group of the Department of Applied Physics at the Aalto University School of Science (until 2010 Helsinki University of Technology), during the years 2007-2011.

My sincere thanks go to Professor Esko I. Kauppinen for offering me the opportunity to work in his group and to complete my dissertation. His scientific expertise and insight, and the challenging environment created in his group, led to fruitful work.

I am especially grateful to my scientific supervisor Dr. Albert G. Nasibulin, for inviting me to work in the Nanomaterials group, offering a challenging topic for my dissertation, and for all his scientific and personal help during my stay.

I am grateful to all my co-authors Dr. Hua Jiang, Dr. Sergey D. Shandakov, Professor Harri Lipsanen, Jani Sainio, Dr. Marco Mattila, Gintare Statkute, Victor I. Kleshch, Dr. Elena D.Obraztsova, Professor Alexander N. Obraztsov, Olga Klimova, Dr. Oleg Tolochko for their efficient work and help with the preparation of articles, valuable suggestions and corrections.

My warm thanks to former and present members of the Nanomaterials group, Larisa I. Nasibulina, Dr. Anton Anisimov, Kimmo Mustonen, Ying Tian, Dr. Prasanta Mudimela, and all the others for their help and the warm working environment they created.

Furthermore, I would like to thank the pre-examiners of my thesis Professor Markku Leskelä and Professor Jorma Jokiniemi.

This study was financially supported by the Academy of Finland (Project Nos. 128445, and 128495).

I am thankful to my parents and brother for support and encouragement during all my studies. Finally, I thank my life companion Olga Urvacheva, for her patience, understanding and positive spirit.

Contents

Thesis publications

1. Nasibulin, A. G., Rackauskas, S., Jiang, H., Tian, Y., Mudimela, P. R., Shandakov, S. D., Nasibulina, L. I., Sanio, J., Kauppinen, E. I., **Simple and Rapid Synthesis of a-Fe_2O_3 Nanowires at Ambient Conditions**, Nano Research **2**, 373-379 (2009).

2. Rackauskas, S., Nasibulin, A. G., Jiang, H., Tian, Y., Statkute, G., Shandakov, S. D., Lipsanen, H., and Kauppinen, E. I., **Mechanistic investigation of ZnO nanowire growth**, Applied Physics Letters **95**, 183114 (2009).

3. Rackauskas, S., Nasibulin, A., Jiang, H., Tian, Y., Kleshch, V., Sainio, J., Obraztsova, E., Bokova, S., Obraztsov, A., and Kauppinen, E., **A novel method for metal oxide nanowire synthesis**, Nanotechnology **20**, 165603 (2009).

4. Kleshch, V. I., Rackauskas, S., Nasibulin, A. G., Kauppinen, E. I., Obraztsova, E. D. and Obraztsov, A. N. **Field emission properties of metal oxide nanowires** Journal of Nanoelectronics and Optoelectronics. (accepted)

5. S. Rackauskas, K. Mustonen, T. Järvinen, M. Mattila, O. Klimova, H. Jiang, O. Tolochko, H. Lipsanen, E. I. Kauppinen and A. G. Nasibulin **Synthesis and doping of ZnO tetrapods for flexible and transparent UV sensors.** (Submitted to Nanotechnology)

Author's contribution

1. The author is mainly responsible for sample preparation, SEM investigation and analysis of the results, co-writing the manuscript (contribution 40%).

2. The author is mainly responsible for the work (except TEM, PL and Raman) and writing the manuscript (contribution 70%).

3. The author is mainly responsible for the work (except TEM, XPS, Raman and FE) and writing the manuscript (contribution 70%).

4. The author is responsible for sample preparation and co-writing (contribution 40%).

5. The author is mainly responsible for the work (except XRD, TEM and PL) and writing the manuscript (contribution 70%).

Other featured publications

1. Rackauskas, S., Jiang H., Wagner J. B., Hansen T. W., Kauppinen E. I. and Nasibulin A. G. **In – situ TEM observation of defect-assisted nanowire growth.** (under preparation)

2. Nasibulin, A. G., Kaskela, A. O., Mustonen, K., Anisimov, A. S., Ruiz, V., Kivistö, S., Rackauskas, S., Timmermans, M. Y., Pudas, M., Aitchison, B., Kauppinen, M., Brown, D. P., Okhotnikov, O. G. and E. I. Kauppinen. **Multifunctional freestanding single-walled carbon nanotube films.** ACS Nano **5**, 3214-3221 (2011).

3. Rackauskas, S., and Snitka, V. **Method for the simple catalytic carbon nano-fibers growth in air**. Microelectronic Engineering 83, 4-9 (2006) 1538-1541.

4. Rackauskas, S. **Carbon nanotube growth and use in energy sector**. Energetika 2, (2006), 43-46.

List of symbols and abbreviations

A	coefficient of proportionality
E	electric field
I	current
J	current density
k_o	pre-exponential coefficient
L	length
E_a	activation energy
R	gas constant
r_g	growth rate
r_m	interstitial migration rate
T	absolute temperature
V	voltage
τ	time
1D	one-dimensional
EDP	electron diffraction pattern
FE	field emission
MBE	molecular beam epitaxy
MOVPE	metalorganic vapor phase epitaxy
NW	nanowire
PET	polyethylene terephthalate
PL	photoluminescence
SEM	scanning electron microscope
TEM	transmission electron microscope
VLS	vapor–liquid-–solid
VS	vapor–solid
XPS	X-ray photoelectron spectroscopy
XRD	X-ray diffraction
ZnO-T	zinc oxide tetrapod

1. Introduction

"There's plenty of room at the bottom."
(R. Feynman, 1959)

Feynman in his famous talk [1] sent an invitation to enter a new field of physics "on a small scale". The possibilities he outlined of building devices out of atoms attracted many researchers to work on this effort. Significant results were achieved only after the invention of microscopes, which are essential for characterization at the nanometer level. Nanometer-scale structures are usually defined as those in which at least one dimension measures less than 100 nm. One-dimensional (1D) representatives of these structures (quantum wires), such as nanowires (NW), have nanometer-scale diameter, but may have lengths of a micron or longer. Owing to this, NWs exhibit extraordinary properties, distinctive from the bulk material, and therefore interest has grown exponentially with the recognition that NWs are an excellent material for nanoscale applications.

Self-assembling growth offers new perspectives on the building and application of nanoscale structures. The vast majority of methods for NW fabrication use vapor–liquid–solid (VLS) growth which has been extensively studied, the main benefit being from the catalyst facilitating structural control. In contrast non-catalytic synthesis has been disregarded and even the possibility of NW growth in the absence of metallic particlesis questioned. However, catalyst-free methods offer the facile fabrication of pure nanowires with fewer technological steps. For the development of non-catalytic techniques an understanding of the growth mechanism is crucial, and so more studies should be focused on the diameter control.

The aim of this thesis was to propose and to develop novel techniques for the non-catalytic synthesis of metal oxide NWs, to examine their structures and properties, and to investigate their growth mechanisms and potential applications. Two different approaches were applied for the synthesis — metal resistive heating and vapor growth methods. The NW growth mechanism during the metal oxidation was studied. The vapor growth method was utilized for the synthesis of ZnO tetrapods. The synthesized NWs were examined for field emission (FE) and ultraviolet (UV) sensing applications.

2. Metal oxide nanowires

In this section, the main synthesis methods for metal oxide NWs and the generally accepted growth mechanisms are briefly introduced.

Metal oxide NWs, or 1D structures also known as whiskers, nanorods, nanobelts or nanoribbons, have been investigated since the late 1960s [2], but received considerable attention only after the nanotechnology boom, and they remain one of the most researched groups of nanomaterials. NWs have demonstrated interesting electrical transport properties that are not seen in bulk materials. This is because electrons can be quantum-confined and thus can occupy discrete energy levels that are different from the energy bands found in bulk materials. And, due to a large surface-to volume ratio, nanowires demonstrate superior sensitivity to surface chemical processes. In addition, their size confinement provides for a tunable band gap, higher optical gain, which makes devices operate faster [3-5]. Moreover metal oxide NWs have an advantage over conventional devices based on semiconductors, as at the nanoscale, the latter materials suffer from the extremely small number of carriers within a device and large phase fluctuations. This serious constraint can be resolved in devices that are based on transition metal oxides because of their orders-of-magnitude greater carrier density (10^{22} to 10^{23} cm^{-3}) [6, 7]. The planar defects, such as twin boundaries and stacking faults, which are typical for non-catalytic NW growth can open new possibilities for other applications, as ordered arrays of planar faults can result in new phases of well known materials with distinct properties. It was shown that the photon energy is tunable by controlling the intervals of the boundaries, without changing the crystal structure and the composition [8, 9]. The control of defect structure in NWs could open up possibilities in optics, similar to doping of pure semiconductors in electronics.

All these and other properties make metal oxide NWs interesting for a number of diverse applications, such as chemical and biosensors [10, 11], field emission devices [12], solar cells [13], water splitting [14], photonics [15, 16], and other electronic and optoelectronic devices [17-19].

2.1 Synthesis methods

During the last decade, 1D metal oxide nanostructures have been extensively investigated. A vast majority of the studies have focused on the synthesis and fabrication of the nanostructures. Typically, two categories of synthesis and fabrication techniques are generally used. One is the so called “bottom-up” techniques using vapor phase deposition, chemical synthesis

or self-assembly. The other is the “top-down” approach utilizing lithography and precision engineered tools for cutting and etching, in order to fabricate nanoscale objects out of bulk materials. In the bottom-up category, several approaches have become well-established, which include the extensively explored vapor phase deposition method, and liquid phase deposition (solution synthesis approach). Another important NW fabrication technique is the application of templates, such as porous alumina or silicon for synthesis. Generally, by this technique NWs are synthesized in the nanopores of a template, which are filled by gas or liquid reactions, and finally the template is removed.

On semiconductor nanostructures, etching processes always lead to significant surface damage, and thus surface states are introduced in the nanostructures; for this reason, self-organized nanostructures are desirable not only in fundamental research but also in future nanodevice design and fabrication [3]. In this work the self-organization method for NW growth was used, and so only the main “bottom-up” techniques will be described.

2.1.1 Epitaxial growth

Molecular beam epitaxy (MBE) isused in semiconductor industry for thin film deposition. By exploiting the surface preparation or catalyst particles these techniques can lead to 1D growth of nanowires.

The MBE technique has been employed to synthesize semiconductor nanowires [20, 21]. Contrary to other synthesis techniques, MBE works under ultra-high vacuum conditions, which allows high-quality semiconductor nanowires to be obtained. The evaporated source atoms or molecules from the effusion cells behave like a beam aimed directly at the substrate (Figure 2.1). NW grow on the substrate which is heated to desired temperature, with the help of catalyst particles. Beams of different material can be supplied. The growth, surface structures and contamination can be monitored *in situ* using reflection high-energy electron diffraction, Auger electron spectroscopy and other surface probing techniques. The NW structure is determined by the catalyst particle preparation, material deposition rate and deposition temperature. The preparation of the substrate surface is also critical for growing high-quality NWs, as the substrate influences the growth direction of the NW. The growth rate of NWs is about 0.1 nm/s (for ZnSe at 530°C) [21].

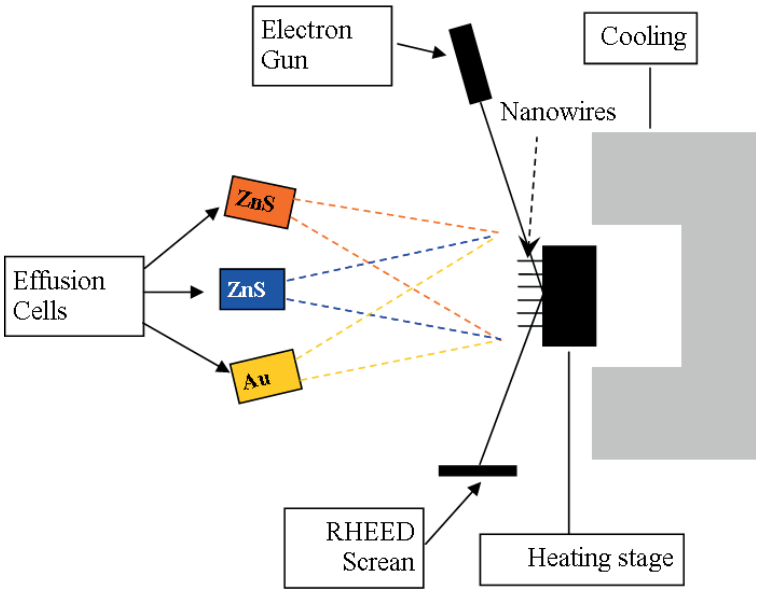

Figure 2.1. Schematic of molecular beam epitaxy growth chamber (RHEED: reflection high-energy electron diffraction).

2.1.2 Metalorganic vapor phase epitaxy

Metalorganic vapor phase epitaxy (MOVPE), also known as metalorganic or organometallic chemical vapor deposition, in contrast to the MBE synthesis of NW, is carried out by chemical reaction and not physical deposition. The precursor is volatile metalorganic or organometallic material, which decomposes at the heated substrate from gas phase. As in MBE, the substrate preparation is crucial for control of the structures obtained. The main defects that often occur in thicker NWs made by these techniques are twin boundaries and stacking faults [21, 22].

2.1.3 Thermal evaporation

NWs and some interesting morphologies of nanostructures such as nano-tetrapods, nanoribbons and comb-like structures [23, 24] can be fabricated by a simple method of thermal evaporation of solid source materials. The experimental setup is shown schematically in Figure 2.2. The temperature gradient and the gas concentration (or vacuum) conditions are two critical parameters for the formation of NWs by this method. Typical materials suitable for this fabrication are metal oxides [25].

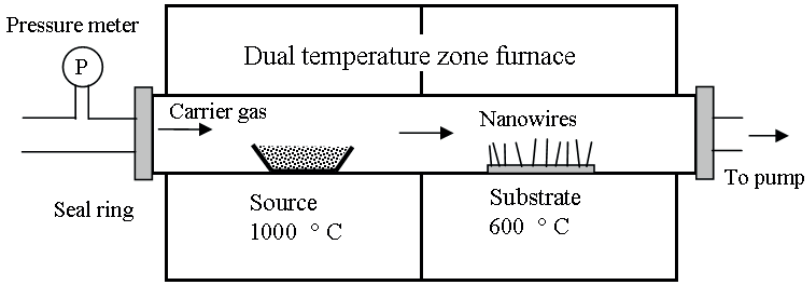

Figure 2.2. An experimental setup of the thermal evaporation method for nanowire synthesis.

The fabrication of these NWs is accomplished by simply evaporating commercial metal oxide powders at elevated temperatures under a vacuum or in an inert gas atmosphere. NW products form in the low temperature regions where materials deposit from the vapor phase. NWs are generated directly from the vapor phase in the absence of a metal catalyst, and this process is often called vapor–solid (VS) growth.

2.1.4 Metal oxidation

It has been known since the late 1960s [2] that if heated at elevated temperatures in an oxidizing atmosphere some metals, such as Cu, Fe, Zn, V, Cr, Nb, W, tend to grow metal oxide NWs on their surface [26-30]. Heating is mostly done in a furnace, but plasma [31] or microwave [32] heating can be also used to lower the synthesis temperature. Metal oxidation is different from the thermal evaporation technique, as high temperatures are not needed and the vapor pressure of a metal or its oxide can be negligible. Moreover, NWs grow directly on the surface of the oxidized metal and vapor transport from source material to substrate is not relevant. Dry or humid oxygen or air is mostly used as the oxidizing atmosphere.

2.1.5 Solution methods

Solution-based 1D material synthesis methods offer the possibility of facile high yield production with low energy consumption and therefore are of interest for industrial application. Typically the process is conducted in an aqueous mixture of soluble metal salts (metal and/or metal–organic) of the precursor materials. Usually the mixed solution is placed in an autoclave at an elevated temperature and relatively high pressure conditions. Typically, the temperature is between 100°C and 300°C and the pressure exceeds 1 atm [33, 34]. Nanocrystals synthesized in aqueous media may often suffer from poor crystallinity, but those synthesized under nonhydrolytic conditions at a high temperature, in general, show much

better crystal quality [35, 36]. Surfactants [37] or templates [38] can be used to obtain 1D structures.

2.2 Growth mechanisms

All growth mechanisms can be generally divided into catalytic growth, where the 1D form of the nanowire is controlled by metallic particles, and non-catalytic growth, where no particles guiding the growth are present.

2.2.1 Catalytic growth

The classical VLS growth mechanism, introduced in a landmark paper by Wagner and Ellis [39], is still applicable for most of the NWs produced today. A schematic view of Si NW growth from Au catalyst is shown in Figure 2.3. VLS is a catalyst-assisted growth process which uses metal nanoparticles as the nucleation seeds. These nucleation seeds determine the interfacial energy, growth direction and diameter of the NWs, so the proper choice of the catalyst is critical. The requirement for VLS growth is a suitable solubility of the constituents of the growing NW within the metal seed particles, and a growth temperature above the eutectic melting point. In the case of growing metal oxide NWs, the VLS process is initiated by the formation of a liquid alloy droplet which contains both catalyst and source metal. Precipitation occurs when the liquid droplet becomes supersaturated with the source metal and under the flow of oxygen, metal oxide NW is formed [40]. Normally the resulting crystal is grown along one particular crystallographic orientation which corresponds to the minimum atomic stacking energy, leading to NW structure formation.

Advances in microscopy, which enabled the growth of NWs to be observed *in situ*, brought new evidence into consideration, questioning the role of the catalyst. The possibility of NW growth under the eutectic temperature was shown [41-44]. Moreover, during the NW growth the catalyst particles were evidenced to be in both solid and liquid state [42, 44, 45], liquid alloy is not required for NW growth [42, 46], therefore the vapor–solid–solid mechanism was introduced [46]. It was also shown that a NW grows in layer-by-layer fashion at the catalyst–NW interface [45, 47].

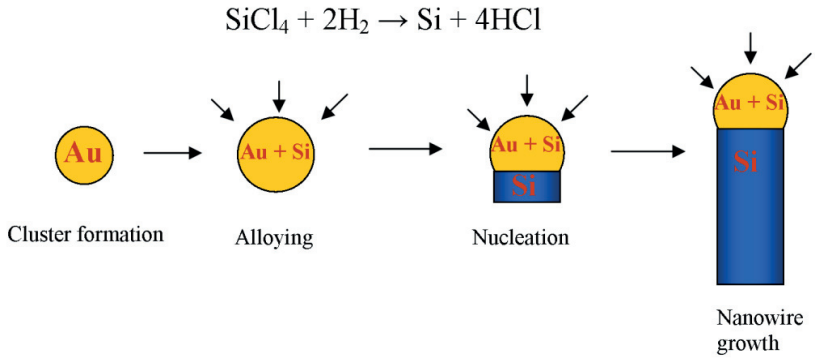

Figure 2.3. The vapor–liquid–solid growth mechanism of Si nanowires gold/silane reaction.

2.2.2 Non-catalytic growth

Non-catalytic growth of NW is less well understood. In the absence of metallic particles that assist the NW growth, the mechanism is interpreted as self catalytic growth. In general, if the NW synthesis involves no catalysts and the process involves vapor condensation, then the process is called VS.

Self catalytic. In self catalytic processes, the metal which is present in the nanowire performs the role of the catalytic particle, so no additional metals are used. The initial droplet for self catalysis is formed from the substrate or from vapor by decomposition or transport [48-51]. For example, MOVPE growth of GaN and InN NW on sapphire has been demonstrated using a single molecule precursor, which during initial decomposition produces metallic droplets that can seed subsequent NW growth [52, 53].

Defect-induced growth. It was first pointed out by Frank [54-56] that perfect crystals would only grow exceedingly slowly. Real crystals grow comparatively rapidly because they contain crystal defects, providing the necessary fast growth front. Line defects, such as screw dislocations with self-perpetuating steps, can provide facile spiral growth fronts for crystal growth when the supersaturation is lower than what is required for crystal growth on perfect crystal facets. This dislocation-driven growth mechanism was proposed in the 1950s by Sears to explain the formation of micrometer-diameter metal whiskers [57, 58]. However, after the original Wagner and Ellis VLS work [39], crystal dislocations were disregarded as the driving force for 1D anisotropic growth. Only recently [59, 60] screw dislocations have been demonstrated to be responsible for tubular and cylindrical NW growth. A NW grown by this mechanism does not depend on catalysts but instead is driven by an axial screwlike dislocation along the length of the NW, providing a continuous growth front for 1D crystal growth, whereas growth on the crystalline side walls is suppressed (Figure 2.4).

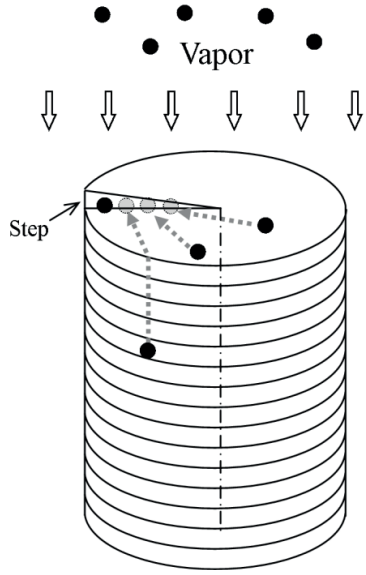

Figure 2.4. A screw dislocation-driven nanowire growth.

It seems plausible that planar defects, such as twin boundaries and stacking faults, could also provide the necessary fast growth fronts. One of the aims of this thesis was to investigate this possibility.

3. Methods

In this section, a brief overview of the NW synthesis methods and characterization techniques used in this work is given.

3.1 Non-catalytic synthesis

Two methods for non-catalytic synthesis were used. First, for a more fundamental understanding and observation of NW growth, a resistive heating method was proposed and examined. Later, for more application-driven research, gas phase synthesis was used, which enabled gram quantities of the NW to be produced.

3.1.1 Resistive heating

Resistive heating, or Joule's heating method, was proposed and elaborated in the framework of this thesis. This method allows pure metal wires to be quickly and controllably heated to the required temperatures.

A schematic of the equipment is shown in Figure 3.1. The synthesis of NWs was carried out under oxidizing conditions by means of the simple resistive heating of as-received pure metal wires or foils suspended between two electric contacts. The temperature was in the range 400—700 °C, and the heating time was from 2s to 10 min. The samples were heated by direct current using a standard laboratory power supply. For heating the substrates to synthesis temperatures, an electric current from 1 to 9 A (corresponding to a power of 2–8 W) was required depending on the material. The wire temperature during the growth was monitored and regulated by an infrared pyrometer (Infratherm IGA 12-s) with a 100 μm measuring spot size. NWs were mostly synthesized under atmospheric conditions without the gas chamber, but also in growth atmospheres of O_2, humid air or low vacuum were used. Ambient air conditions corresponded to regular laboratory and atmospheric pressure conditions with a temperature from 21 to 24 °C and a relative humidity from 20 to 45%. The NWs were absent only at both ends of the wire due to the heat losses and, as a result, the lower temperature in the vicinity of the contacts.

Metal wires 0.25 mm in diameter or foils with 0.1–0.04 mm thickness were used as substrates. Mo (99.97%), Cu (99.999%), W (99.9+%) and Ti (99.6+%) wires were purchased from Aldrich Chemical, and Co, Zn (both 99.99+%), Fe (99.99% and 99.5%), V (99.8%), Ni (99.98%), Pd (99.9%), Sn (99.99+%) and In (99.999%) wires were purchased from Goodfellow Cambridge Ltd. Characterization of the samples was done without any post-

processing. For transmission electron microscopy (TEM) investigations, the NWs were dry transferred by pressing samples on TEM grids.

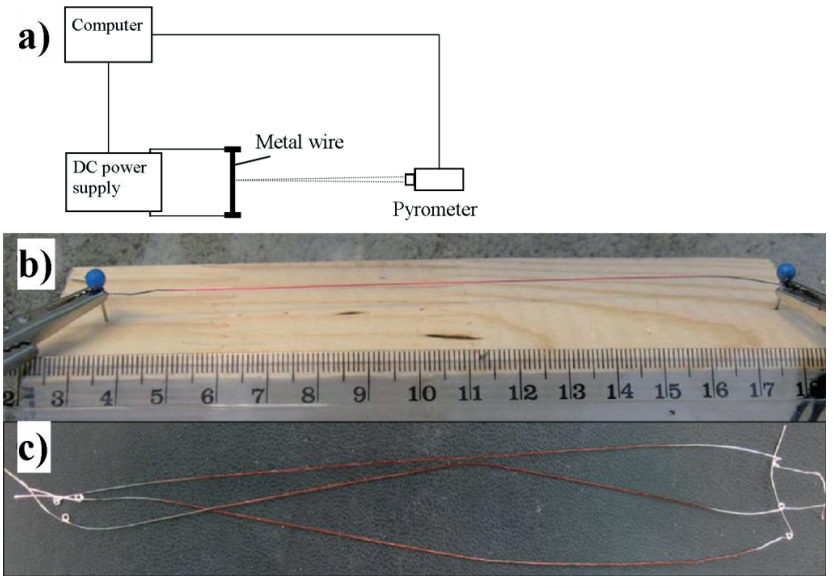

Figure 3.1. Resistive heating equipment: a) schematic illustration; b) photo of nanowire synthesis process; c) Fe wires treated for 3 min under ambient air conditions.

3.1.2 Gas phase synthesis

The synthesis reactor consisted of a vertical quartz tube inserted in a furnace, a metal evaporator inside the tube and the product collection system (Figure 3.2). A vertical orientation of the reactor was used to minimize recirculation associated with the buoyancy forces. The metal evaporator was a stainless steel tube filled with Zn powder (99.999% purity) mixed with SiO_2 carrier granules (99.99% purity) of 0.2—0.7 mm in size. 1 g of the mixture, consisting of 2/3 wt. % zinc and 1/3 wt.% SiO2, was placed on a supporting net in the evaporator. The temperature of the evaporator was measured using a K-type thermocouple, mounted underneath the supporting net. The position of the evaporator was adjusted so that its temperature was the same as the furnace temperature. Argon (99.999%), purified from an oxygen species by an oxygen trap (Agilent OT3-4), was utilized as the carrier gas through the evaporator at a flow rate of 0.3 L/min. An outer air flow was introduced in the reactor at a flow rate of 1.0 L/min. The flow behavior was maintained to be laminar with the Reynolds number varying from 220 to 330 depending on the experimental conditions. The average residence time in the reactor varied from 1.9 to 2.6 s. Product was collected downstream of the reactor on a nitrocellulose filter with a pore size of 0.45 μm.

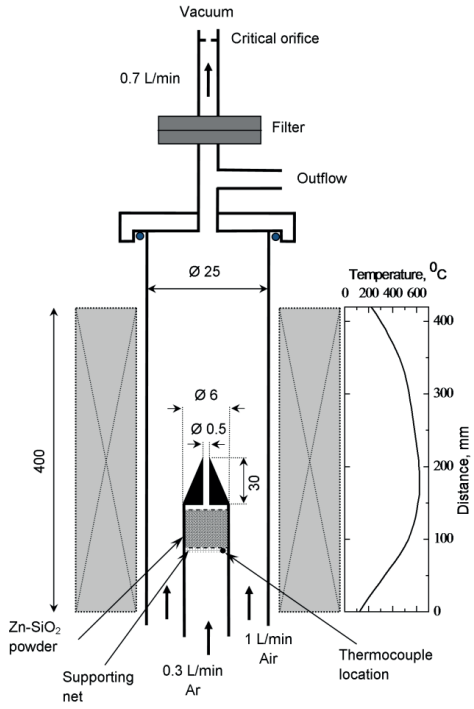

Figure 3.2. Schematic view of the vertical flow reactor. Dimensions are given in mm.

3.2 Characterization

3.2.1 Electron microscopy

In this work, scanning electron microscopy (SEM) and high-resolution TEM were used for structural sample characterization.

3.2.1.1 Scanning electron microscopy

A simplified illustration of the SEM imaging process is shown in Figure 3.3a. A beam of electrons is emitted from an electron source, by either field or thermionic emission, with primary electron energies of 1—15 keV. The beam is shaped using electromagnetic condenser lenses and focused on the sample by the objective lens. The focused spot is scanned on the sample using a coil, and secondary electrons emitted by atoms near the measurement spot are detected. The final image is formed by combining position information from the scanning coil driver with the detector signal. Back-scattered electrons can also be used for imaging. The resolution of SEM is typically a few nanometers, and it gives a good general overview of the surface density of NWs, their length and growth orientation.

SEM measurements were made with a Leo 982 Gemini microscope and a JEOL JSM-7500F microscope.

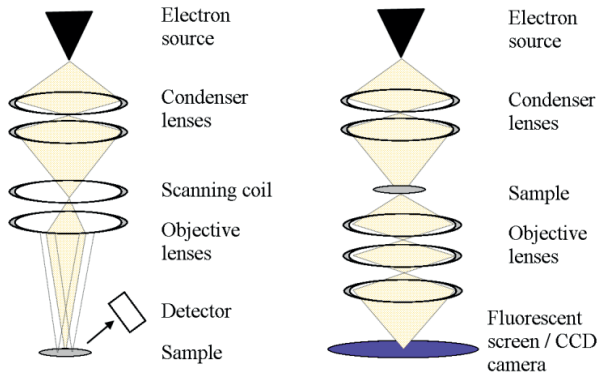

Figure 3.3. Simplified schematic diagrams of a) scanning electron microscope and b) transmission electron microscope.

3.2.1.2 Transmission electron microscopy

A schematic view of TEM is shown in Figure 3.3b. A parallel beam of electrons emitted by an electron gun is focused by a condenser lens onto the sample. The electron beam travels through the specimen, and some of the electrons are scattered. The transmitted portion is focused by an objective lens to project a magnified image onto a screen.

As an additional TEM technique, electron diffraction (ED) is used to study matter by firing electrons at a sample and observing the resulting interference pattern arising at the sample which arises from the wavelike nature of electrons. The periodic structure of a crystalline solid acts as a diffraction grating in scattering electrons. Analysis of the observed diffraction pattern gives information on the structure of the crystal, producing the diffraction pattern. TEM and ED observations were carried out with a Philips CM200 microscope and a JEOL-2200FS double aberration-corrected microscope, both operated at 200 kV.

3.2.2 Optical characterization

3.2.2.1 Optical absorption spectroscopy

In optical absorption spectroscopy, the absorption of light as a function of frequency or wavelength is measured. The sample absorbs photons from the incident light, and the intensity of the absorption varies as a function of frequency.

In this work, the absorption spectra of ZnO tetrapods (ZnO-Ts) were measured using a double line UV-visible-near infrared spectrophotometer (Perkin-Elmer lambda 900). ZnO-Ts were sonicated in ethanol and then transfered onto a quartz substrate for absorbance measurement.

Wavelengths from 250 nm to 800 nm were used for the optical absorption spectroscopy.

3.2.2.2 Photoluminescence

Photoluminescence (PL) is a tool for contactless and nondestructive probing of the electronic structure of materials. Photo-excitation causes electrons within the material to move into allowed excited states. When these electrons return to their equilibrium states, the excess energy is released and may include the emission of light (a radiative process) or may not (a nonradiative process). The energy of the emitted light (PL) relates to the difference in energy levels between the two electron states involved in the transition between the excited state and the equilibrium state.

PL measurements were carried out at room temperature using a HeCd laser operating at 325 nm for excitation at an average intensity of about 20 W/cm^2. The sample PL was spectrally resolved in a monochromator and detected using a photomultiplier tube and lock-in techniques.

3.2.2.3 Raman spectroscopy

Raman spectroscopy is a spectroscopic technique based on inelastic scattering of monochromatic light, usually from a laser source. Inelastic scattering means that the frequency of photons in monochromatic light changes upon interaction with a sample. Photons of the laser light are absorbed by the sample and then reemitted. Frequency of the reemitted photons is shifted up or down in comparison with the original monochromatic frequency, which is called the Raman effect. This shift provides information about vibrational, rotational and other low frequency transitions in molecules.

Raman spectra were obtained with a Wintech alpha300 spectrometer using a frequency doubled Nd:YAG green laser (λ = 532 nm). In order to minimize possible sample degradation, a low laser power of about 160 μW was used for the measurements.

3.2.3 X-ray techniques

3.2.3.1 X-ray photoelectron spectroscopy

X-ray photoelectron spectroscopy (XPS) is a quantitative spectroscopic technique that measures the elemental composition, empirical formula, chemical state and electronic state of the elements that exist within a material. XPS spectra are obtained by irradiating a material with a beam of X-rays while simultaneously measuring the kinetic energy and number of

electrons that escape from the top 1 to 10 nm of the material being analyzed. XPS requires ultra high vacuum conditions.

XPS was carried out with a Surface Science Instruments SSX-100 ESCA spectrometer using monochromatic Al Kα x-rays (1486.6 eV). Core-level spectra were recorded with a pass energy of 60 eV and an X-ray spot size of 300 μm. The binding energy scale was referenced to the characteristic carbon 1s binding energy of 285 eV.

3.2.3.2 X-ray diffraction

X-ray diffraction (XRD) is a technique used to characterize the crystallographic structure, crystallite size (grain size), and preferred orientation in polycrystalline or powdered solid samples. XRD is based on observing the scattered intensity of an X-ray beam hitting a sample as a function of incident and scattered angle, polarization, and wavelength or energy.

In this work the crystalline structure of the ZnO-Ts was examined via XRD (using a Bruker D8 Advance diffractometer), with Cu Kα X-rays scanning angle 25 – 60 2θ.

4. Results and discussion

4.1 Synthesis and properties

4.1.1 Resistive heating

In this work a non-catalytic method for the rapid growth of metal oxide NWs by oxidation under ambient conditions is proposed and elaborated. In order to demonstrate the simplicity and rapidness of our method we selected four metals: Fe, Cu, V and Zn (Figure 4.1). The successful NW synthesis was carried out in the 400—700 ^{o}C range , i.e. at temperatures below the melting temperature of the metals used, except Zn. A resistive heating of the wires and foils provided uniform temperature distribution in their middle parts.

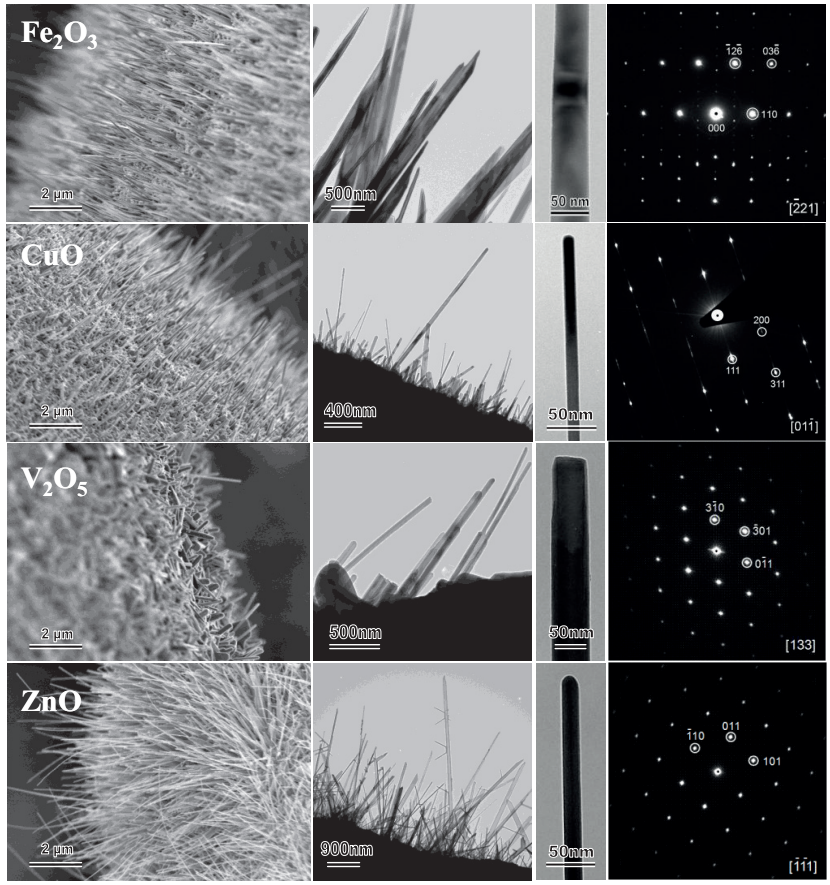

Figure 4.1. The results of electron microscopy investigations of Fe_2O_3, CuO, V_2O_5 and ZnO nanowires (NWs). Columns from left to right, respectively, show scanning electron micrographs of NWs, low and intermediate magnification transmission electron micrographs of NWs, and electron diffraction patterns with indexes that determined their crystal structure.

The middle part of the wire (foil) surfaces was evenly covered by NWs. The areas in the vicinity of contacts had lower temperatures due to the heat losses and thereby did not contain NWs. The surface of the wire was oxidized and layers of metal oxides were formed (Figure 4.2).

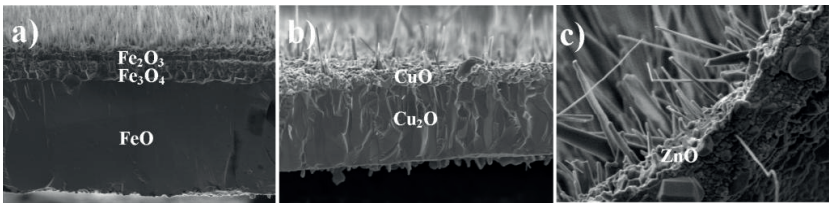

Figure 4.2. Scanning electron micrographs of metal oxide layers on the surface of different metals: a) iron; b) copper; c) zinc.

SEM and TEM observations showed that the NWs produced were preferentially orientated perpendicular to the substrate surface. Electron diffraction experiments were carried out to investigate the structures of the NWs using their electron diffraction patterns (EDPs) and these are shown in Figure 4.1. Those EDPs were indexed as orthorombic Fe_2O_3 (a=0.503nm, c=1.375nm), monoclinic CuO (a=0.469nm, b=0.342nm, c=0.513nm), orthorhombic V_2O_5 (a=1.154nm, b=0.438nm, c=0.357nm) and hexagonal ZnO (a=0.325nm, c=0.521nm). In the case of Fe wire, blade and rod-like Fe_2O_3 NWs were synthesized (Figure 4.2). The NWs were from 1 to 5 μm long with the highest density on the substrate surface at synthesis temperatures from 690 to 720 ºC. CuO NWs with the highest density on Cu foils and wires were formed in the temperature range 420–480 ºC. The CuO NWs had rod shapes with diameters from 20 to 50 nm and with lengths from 0.5 to 2 μm. Resistive heating of V wires and foils at ambient conditions in the temperature range 450–480 ºC resulted in the highest density of V_2O_5 NWs. V_2O_5 NWs had rod-like structures with diameters of 50–60 nm and lengths of 0.5–1 μm. Oxidation of Zn wire led to the formation of ZnO NWs in a wide temperature range from 500 to 700 ºC with a diverse morphology. At lower temperatures (500–600 ºC) mainly rod-like and belt-like NWs with diameters of 8-–20 nm and lengths of 1–10 μm were observed; some NWs were branched. Increasing the synthesis temperature to about 700 ºC resulted in the formation of blade-shaped NWs of 1–5 μm in length. From the SEM images the highest density of surface coverage was observed for Fe_2O_3 and ZnO NWs and the lowest for CuO and V_2O_5 NWs.

The chemical composition of the substrate wires after the synthesis was evaluated by Raman spectroscopy measurements (Figure 4.3). The spectrum obtained from the iron oxide NWs is shown in Figure 4.3a. Peaks,

located at 225, 245, 292, 411, 498, 611 and 1323 cm^{-1}, correspond to α-Fe_2O_3. The presence of a small amount of Fe_3O_4 could be also detected as a peak at 663 cm^{-1} [61, 62]. The Raman modes originating from CuO and Cu_2O were both observed in the spectrum measured for Cu wire (Figure 4.3b). The peaks at about 298, 342, 633 cm^{-1} correspond to the A_g, B_g^1 and B_g^2 modes of CuO, respectively [63, 64]. The peaks at 219, 342, and 411 were assigned to Cu_2O. There is also a contribution from Cu_2O to the band centered at around 633 cm^{-1}, which makes this peak broader and more intense than for pure CuO [65-68]. The small shift in Raman frequency and profile broadening could be caused by the nanocrystalline structure [69]. The Raman spectrum of NWs grown on V wire showed two kinds of vanadium oxides with oxidation state of +5 and +4 (Figure 4.3c). Peaks at about 146, 194, 281, 309, 479, 525, 699, 994 cm^{-1} and at 403 cm^{-1} visible as shoulder could be indexed to V_2O_5 [70-72]. Raman modes from VO_2 can be also seen at 222, 339, 392, 446, 498, and 614 cm^{-1}. The peaks at 194 and 309 cm^{-1} are contributed to by both V_2O_5 and VO_2, consequently they are more intense [73, 74]. The Raman spectrum of zinc oxide NWs (Figure 4.3d) reveal a peak centered at 438 cm^{-1}, which corresponds to the E2 mode of ZnO [75]. The Raman scattering peak at 561 cm^{-1} is related to the oxygen deficiency in ZnO [76].

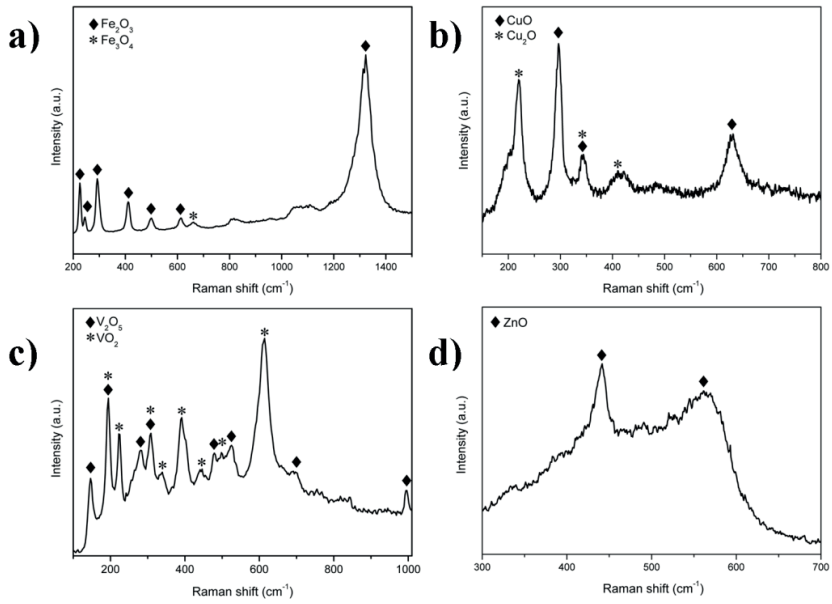

Figure 4.3. Raman spectra obtained from different metal oxide NWs: a) iron oxide; b) vanadium oxide; c) copper oxide; d) zinc oxide.

The chemical composition of the surface layer with NWs was confirmed by XPS. The chemical state of Fe wire can be determined from the Fe 2p

spectrum shown in Figure 4.4a. The Fe $2p_{3/2}$ maximum was found at approximately 710 eV and the satellite peak between the $2p_{3/2}$ and $2p_{1/2}$ peaks around 719 eV [77]. The positions of these peaks as well as the shape of the Fe 2p spectrum agree closely with the Fe^{3+} state characterization reported by Aronniemi *et al.* [78]. The Cu 2p spectrum for copper oxide NWs is shown in Figure 4.4b. The observed $2p_{3/2}$ binding energy corresponds to CuO. The multiple peaks observed are typical for the CuO phase and can be interpreted as metal–ligand charge transfer satellites [77, 79]. XPS spectra of vanadium oxide nanorods (Figure 4.4c) show a mixture of different oxidation states, mainly V^{5+} and V^{4+}, but also small amounts of V^{3+} could be present. An analysis of V 2p spectrum [80] revealed that the atomic concentrations of V^{5+} and V^{4+} as percentages of total vanadium were about 85% and 15%, respectively. Figure 4.4d shows the Zn 2p region and the LMM Auger region measured to characterize zinc oxide. The Auger parameter was utilized for the characterization, since the Zn and ZnO 2p binding energy values are very close. The Auger parameter was calculated as the sum of the Zn $2p_{3/2}$ binding energy and the Auger $L_3M_{45}M_{45}$ kinetic energy to be 2010.2 eV, which is typical for ZnO [79]. The calculated atomic ratio of Zn and O also supports the oxidation of Zn wire to ZnO.

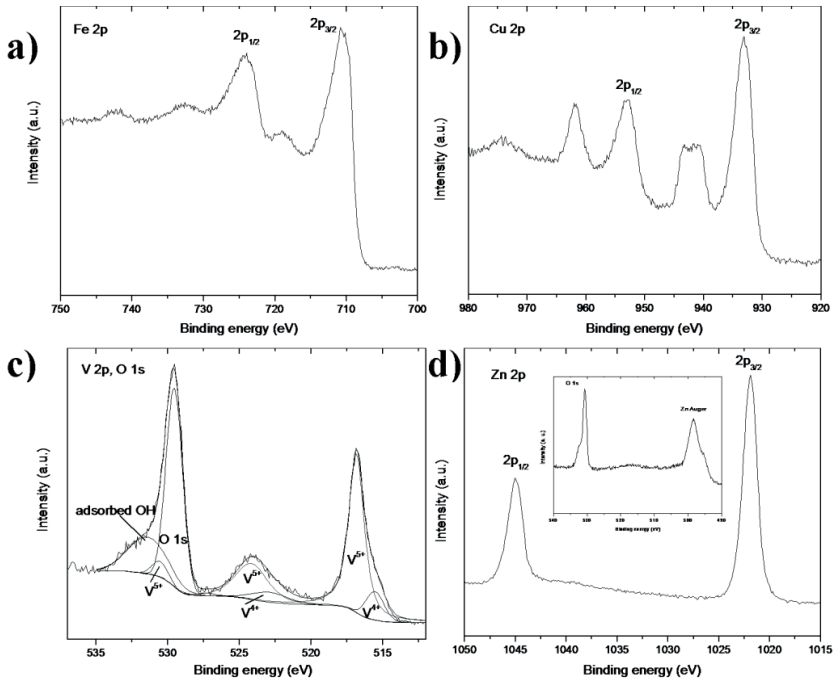

Figure 4.4. X-ray photoelectron spectra obtained from different metal oxide nanowires: a) Fe 2p region of iron oxide sample; b) Cu 2p spectrum of copper oxide sample; c) V 2p and O 1s region of vanadium oxide sample with fitting; d) Zn 2p region of zinc oxide sample.

From TEM, Raman and XPS measurements it can be concluded that metal wires are covered by NWs of the corresponding metal oxide. NWs were indexed by EDP as Fe_2O_3, CuO, V_2O_5 and ZnO. Peaks from several oxides appear in Raman spectra; however, XPS shows only one metal oxide (except for vanadium): Fe_2O_3, CuO and ZnO. This can be explained by the different depth resolutions of these two methods. Raman depth resolution is in the range of a micron, whereas the XPS signal comes from only the few topmost atomic layers. Nevertheless, the presence of small amounts of lower oxidation state metal oxides on the surface cannot be excluded, as the sensitivity limit of XPS is about one per cent.

For investigations of NW growth kinetics, we applied a potential difference to the wires (to heat them to the optimum temperature) for a certain period of time. After this the wires were rapidly cooled down by switching the power off. In the case of Fe, after only 2-4 s, α-Fe_2O_3 NWs of about 200 nm in length were found on the surface of the treated wires (Figure 4.5a). The growth of α-Fe_2O_3 NWs was therefore found to be very rapid and the rate was estimated to exceed 100 nm/s. A dense NW "forest" was produced after 40 s and no changes were observed after longer heat treatment times. Similar investigations carried out with Zn, V and Cu revealed the presence of NWs after just 10 s treatment time.

A non-catalytic method for the rapid growth of metal oxide NWs by oxidation at ambient conditions is demonstrated. This method is very simple and does not require any expensive and complicated equipment. In the simplest approach, the NWs could be grown at ambient conditions using a car accumulator or a set of household batteries. The NW growth required 2—8 watts of energy for a 3 cm long sample, which is a thousand times less than the energy consumed during conventional synthesis methods. Usually the growth of dense NW forest takes a few hours [10, 15-19], while in our case 40 s was enough to completely cover the surface of the substrate. The growth rate of the iron oxide NWs exceeded 100 nm/s, which is to the best of our knowledge the highest rate so far reported. This high growth rate can be explained by the temperature profile across the wire and the high heating rate: in our method the wire was heated from inside and very quickly produced a higher temperature gradient across the wire than the conventional furnace oxidation techniques. Thus, the resistive heating method for the growth of NWs is the most simple and rapid one.

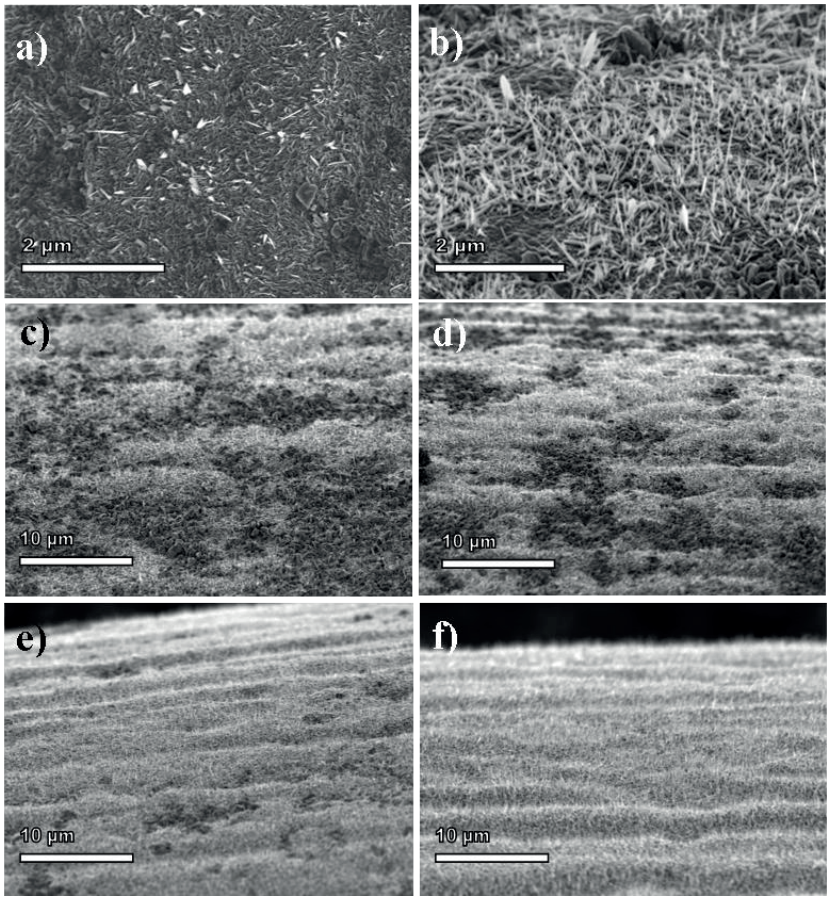

Figure 4.5. Scanning electron micrographs of the iron wire surface after different synthesis times: a) 2 s; b) 8 s; c) 15 s d) 20 s; e) 30 s; f) 35 s.

4.1.2 Gas phase synthesis

The aim of this sinthesis technique study was to growth tetrapods with high aspect ratio legs and to investigate the growth mechanism. ZnO-Ts were synthesized by a gas phase oxidation of Zn vapor in an air atmosphere in the temperature range 500 – 800 °C. At temperatures of 500 °C and below, only particles with diameters of 50—200 nm were produced (Figure 4.6a). It can be seen that some particles had short tetrapod legs (inset in Figure 4.6a). At a temperature of 600 °C, an increase in the Zn partial pressure resulted in a drastic change in the particle morphology: from nearly spherical particles to thick and short leg tetrapod structures (Figure 4.6b). From the leg structure one can assume the screw dislocation growth mechanism was operating, as was shown for ZnO nanowires [60]. A further increase in the temperature to 700 °C led to ZnO-Ts with high aspect ratio legs (diameters of 10—20 nm and lengths up to 0.5 µm) as shown in Figure 4.6c. From the TEM image presented in Figure 4.7a it can be seen that each

ZnO-T leg was a single crystal. Increasing the temperature to 750 °C caused the formation of polycrystalline plates on ZnO-T legs (Figure 4.7b).

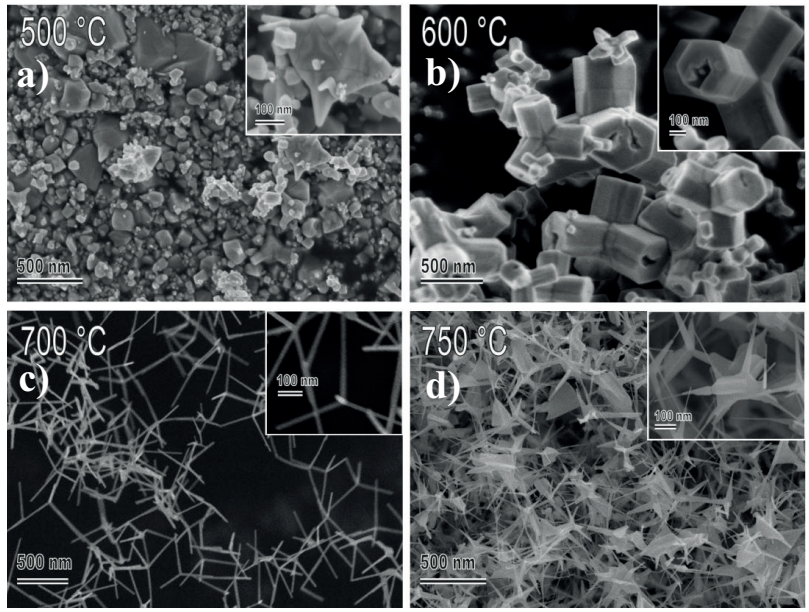

Figure 4.6. Scanning electron micrographs of ZnO structures synthesized at different temperatures. Insets are close up images.

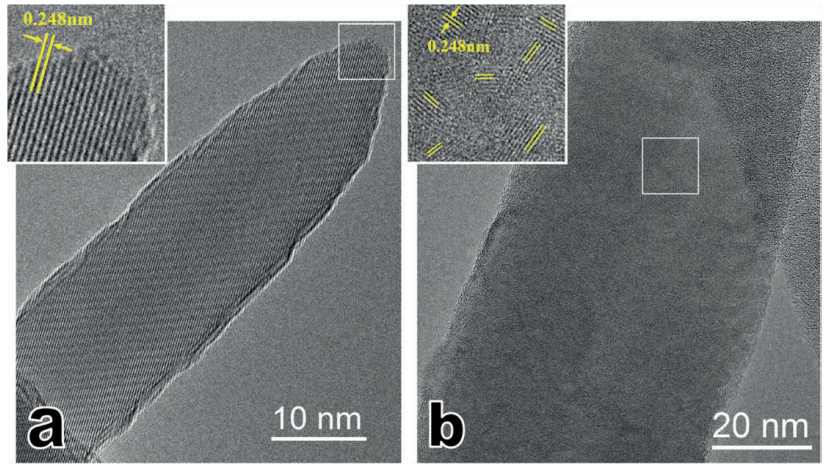

Figure 4.7. High resolution-transmission electron micrographs of zinc oxide tetrapod legs, synthesized at: a) 700 °C, b) 750 °C. Insets are the close ups, showing lattice fringes.

4.2 Growth mechanism

4.2.1 Nanowire growth by resistive heating

Resistive heating synhtesis was investigated for CuO, Fe_2O_3, V_2O_5 and ZnO NW, which all follow the same growth mechanism. Mechanistic growth

investigation was done for ZnO NWs, and growth mechanism was demonstrated with the example of Fe_2O_3 NW growth.

4.2.1.1 ZnO nanowire mechanistic growth investigation

In order to investigate the kinetics of the NW growth, we prepared samples of ZnO NW by resistive heating at different temperatures with a fixed growth time of 1 minute. The lengths of the NWs measured from SEM images were used for the calculations of the average growth rate (Figure 4.8a). Two regions can be clearly distinguished in this plot: the kinetic and constant growth rate regions. In the kinetic region, the average NW growth rate increased with the temperature rise until 803 K. At higher temperatures the NW growth rate remained nearly constant. It is worth noting that the surface density of the NWs significantly decreased at higher temperatures. The ZnO NW shape also underwent a change in shape from rod-like at temperatures ≤ 803 K to sword-like at temperatures above 850 K.

Also, we examined the kinetics of ZnO NW growth at the fixed temperature of 803 K, where the growth rate is the highest. It is known that during Zn oxidation the ZnO layer thickens according to the parabolic law [81, 82], which is associated with the diffusion of Zn vacancies and interstitials [83]. The vacancy and interstitial migration rate r_m can be expressed as:

$$r_m = A\tau^{-0.5}, \tag{4.1}$$

where A is a coefficient of proportionality and τ is time. Plotting the kinetic data of the ZnO NW growth rate r_g at 803 K using the coordinates ln r_g – ln τ gives a similar linear dependence (Figure 4.9b):

$$\ln r_g = -0.4721 - 0.5095 \ln \tau, \tag{4.2}$$

Consequently it can be concluded that the NW growth rate r_g also has parabolic time dependence. This indicates that ZnO NW growth is determined by the migration of Zn vacancies or interstitials.

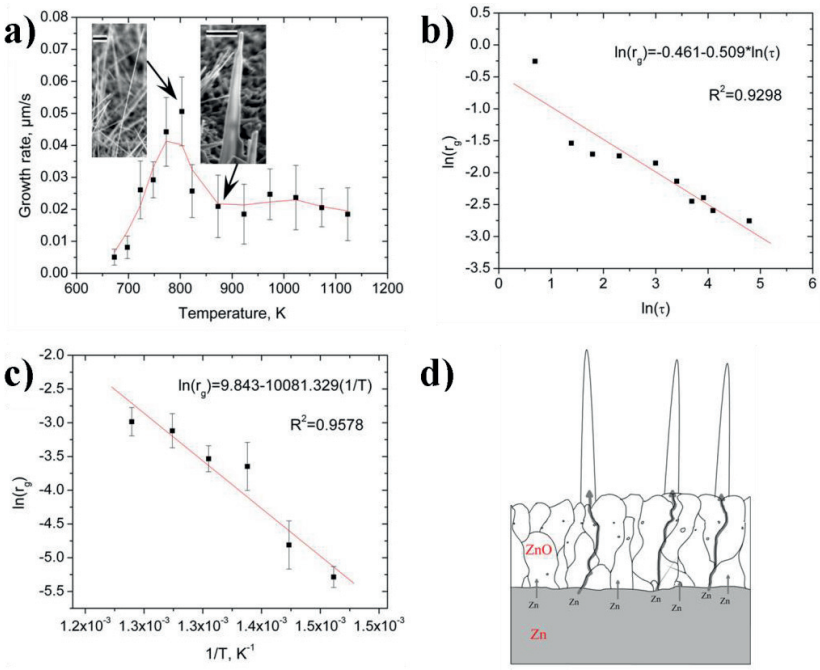

Figure 4.8. Kinetic data of ZnO nanowire (NW) growth: a) growth rate dependence on the process temperature and scanning electron micrographs of ZnO NWs at indicated temperatures (scale bar 500 nm); b) growth rate (μm/s) dependence on time (s) in a double logarithmic scale; c) kinetic region (673–803 K) data of the growth rate in the Arrhenius coordinates; d) schematics of ZnO NW growth mechanism.

The rate of ZnO NW growth can be expressed by the Arrhenius dependence,

$$r_g = \frac{dL}{dt} = k_0 \exp\left(-\frac{E_a}{RT}\right), \qquad (4.3)$$

where L is the length of NW; k_0 is the pre-exponential coefficient; E_a is the activation energy of the NW growth; R is the gas constant; T is the absolute temperature. Furthermore, plotting the kinetic region (673–803 K) data of the growth rate in the Arrhenius coordinates ln r_g – $1/T$ gives a linear dependence (Figure 4.8c), from which the activation energy was found to be E_a = 83.8 kJ/mol. This value can be attributed to the migration energy of the Zn interstitials and vacancies (77 and 88 kJ/mol, respectively [84]). Migration of oxygen interstitials is less probable because of oxygen's larger size. Indeed, oxygen interstitial and vacancy migration energies are 118 and 124 kJ/mol, respectively [84]. The activation energy for ZnO lattice diffusion is as high as 305 kJ/mol [82, 83] and, as a result, cannot be attributed to the limiting stage of the NW growth. Therefore, it can be deduced that the growth of ZnO NWs complies with the parabolic law and is determined by zinc interstitial and vacancy migration.

Based on the oxidation mechanism and our investigations, the following ZnO NW growth mechanism can be proposed. According to the metal oxidation mechanism [82, 84, 85] zinc oxidation involves Zn diffusion from the Zn-ZnO interface to the surface (Figure 4.8d). Advantageous diffusion through grain boundaries compared to lattice diffusion [83, 84] creates sites on the surface, from which ZnO NWs grow. Rod-like shaped ZnO NWs are created through anisotropic Zn diffusion in the direction of energetically favorable crystal growth [110]. The optimum growth conditions for a dense ZnO NW "forest" occur at 803 K. At temperatures ≥ 850 K, the size of the ZnO grains becomes larger [86], so that there is less grain boundary space for rapid diffusion to occur. This is confirmed from SEM images as the density of ZnO NWs on the surface at temperatures above 803 K is lower.

The growth of the ZnO NWs is also determined by the presence of defects such as stacking faults. The amount of the synthesized NWs was drastically reduced when the temperature was above 803 K, which is likely to be explained by the formation of the NWs with higher crystallinity. TEM and PL investigations confirmed the presence of fewer defects and lower surface NW density at higher synthesis temperatures. However, the annealing of ZnO NWs at high temperatures should not be neglected, since NWs appear on the surface after only 10 s.

4.2.1.2 Nanowire growth mechanism by resistive heating method

The mechanism for metal oxide NW growth was obtained on the basis of our experimental results and literature data. Growth mechanism is similar for all NWs grown by resistive heating method, and it is demonstrated taking Fe_2O_3 as an example. The formation of NW occurs when oxide layers are gradually formed by oxidation of the metal (Figure 4.2.). The growth of NWs is determined by diffusion processes. The driving force determining the motion of metal and oxygen ion species is the potential difference that appears during the wire oxidation process (Figure 4.9). The electric field strength between iron and Fe_2O_3 layers can reach values as large as 10^6 V/cm [87]. It is worth noting the electric field arising during resistive heating of an iron wire is about six orders of magnitude lower and thereby cannot significantly affect the ion motion across the wire. The metal oxidation process involves the diffusion of metal ions from the iron wire core to the surface through the metal oxide layers and of oxygen ions in the opposite direction [87, 88]. At certain temperatures, grain boundaries in the metal oxide layers, likely formed due to the oxidation stress, could be responsible for a higher diffusion rate compared to the lattice diffusion [88]. In the initial stage, the Fe_2O_3 phase might grow in all directions;

however, only the [110] crystallographic direction endures due to its energetically favorable conditions [28], such as easier diffusion and advantageous stacking. It is worth noting that the presence of stacking faults in the growth direction supports our explanation of the mechanism, since the diffusion rate is enhanced in the crystal defects at elevated temperatures [89, 90]. Another path for iron ion delivery to the top of the growing NW is surface diffusion. The NW sword-like shape confirms that the growth is determined by diffusion process from the bottom, where the NWs are thicker, to the top, where they become thinner. The growth of NW terminates as metal oxide layers become too thick for charge transfer or ion diffusion. Typical length of NWs grown by resistive growth method is 1 to 5 μm for synthesis time of 3 min. The same growth mechanism is valid also for other metal oxidation synthesis techniques.

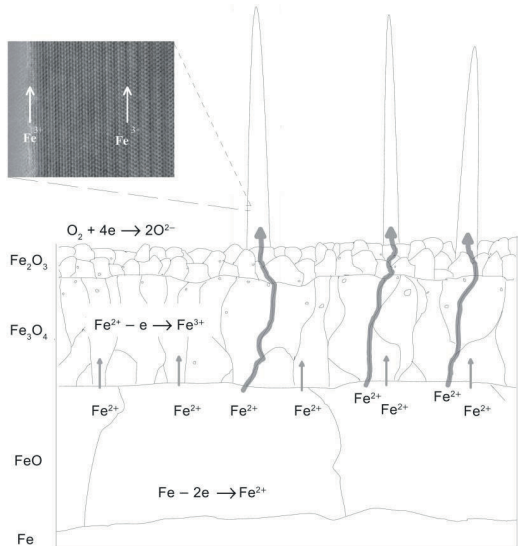

Figure 4.9. Schematic presentation of the nanowire growth in ambient air conditions.

4.2.1 ZnO tetrapod growth mechanism

The growth of tetrapod structures of ZnO [91] and other II-IV semiconductors [92] has been explained by the formation of the zinc blende nucleus, out of which wurtzite legs grow [93]. The formation of such highly anisotropic shapes as tetrapods requires a kinetic growth regime where the rate of the monomer arrival is greater than its diffusion on the surface [92, 94]. At low growth rates, under thermodynamic control, spherical nanocrystals are formed. When the growth rate is increased, preferential growth at most reactive sites is expected.

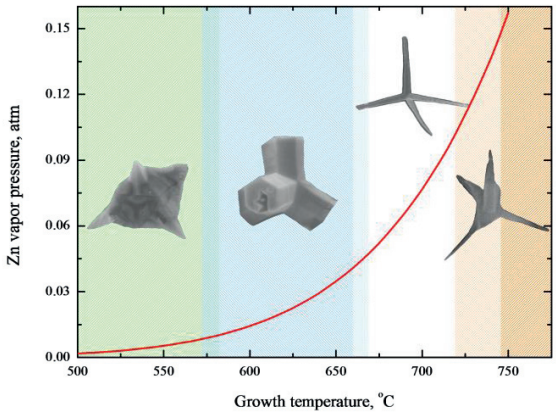

Figure 4.10. Morphology of zinc oxide tetrapods at different temperatures and vapor pressures. Tetrapods shown are not to scale.

The overall trend in morphological change of the ZnO-Ts is summarized in Figure 4.10. From our experimental data one can see that at 500 °C there is not significantkinetic growth — only very few particles had anisotropic growth sites and grew short tetrapod legs. At 600 °C, the Zn partial pressure increased and a higher growth rate and anisotropic structures are observed (Figure 4.6b). However, even at 600 °C, the Zn vapor pressure is low, which favors a higher nucleus diameter and also a lower kinetic growth rate, and consequently resulted in ZnO-T structures with low aspect ratios. At 700 °C highly anisotropic structures were obtained because of the high Zn vapor pressure, favoring small nucleus diameters and fast kinetic growth. When the temperature was further increased, a large number of small diameter particles were produced, which further aggregated into polycrystalline plates (Figure 4.6d and Figure 4.7b) having a nearly ordered structure in one direction. Such spontaneous oriented attachment of primary particles is explained by oriented aggregation, which is caused by a substantial reduction in the surface free energy [95, 96].

4.3 Applications

FE applications of NW grown by resistive heating and UV sensor applications of ZnO-T grown by gas phase synthesis are shown in this section.

4.3.1 Field emission

FE is emission of electrons induced by an electrostatic field, usually from a solid surface into a vacuum. FE occurs in high electric fields and is strongly dependent upon the work function. Needle-like nanoscale arrays are

expected to possess low voltage field electron emission properties due to the electric field enhancement effect on the nanostructured tips [97].

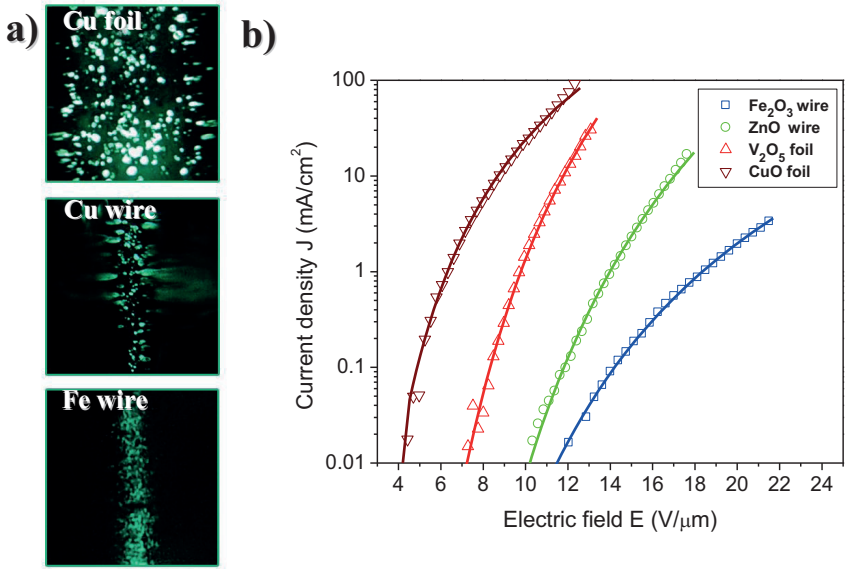

Figure 4.11. Field emission properties of metal oxide nanowires (NWs): a) typical images of the field emission pattern (frame size 5×5 mm) on the luminescent screen for the copper foil (top), copper wire (center) and iron wire (bottom); b) current density versus electric field strength (*J-E*) for the samples with different types of metal oxide NWs. The solid lines are the Fowler─Nordheim approximations of the experimental points.

For measurements of FE properties the samples were placed in a vacuum diode FE set-up and used as cathodes. The FE current–voltage characteristics were obtained by applying a pulsed voltage between electrodes up to 10 kV with a pulse duration of about 15 μs and with a repetition frequency of 200 Hz. The middle parts of the foils or wires 1 cm long were mounted on steel substrates parallel to a flat anode. To characterize the spatial distribution of the emission sites over the sample surface a conductive cathodoluminescent screen was used as the anode. The distance between electrodes was varied from 100 to 500 μm with a high precision screw translator.

The samples were used without any pretreatment as cathodes in a vacuum diode FE setup. In order to compare the results obtained for different samples the current-voltage (I-V) curves were converted to current density dependencies on an electric field (J-E). The electric field intensity, *E*, in the diode was defined as a ratio of the applied voltage, *V*, to the inter-electrode distance. The current density, *J*, is defined as a ratio of the cathode current,

I, to the emitting cathode area, estimated from the emission pattern on the luminescent screen. The FE patterns obtained for the wires and foils were quite homogeneous for all types of metal oxide samples (Figure 4.11a). The J-E dependencies of samples with NWs are presented in Figure 4.11b. The approximation of J-E curves with the Fowler—Nordheim equation gives a good agreement with the tunneling mechanism of emission [98].

The samples with CuO NWs showed the best FE characteristics. The threshold field value corresponding to the current density of 0.01 mA/cm^2 was about 4 V/μm. The maximum current density for samples with CuO NWs was about 100 mA/cm^2. These parameters are comparable with the best FE characteristics reported for different metal oxides structures in Refs [99-102]. V_2O_5, ZnO and Fe_2O_3 NWs have higher threshold fields and lower maximum current densities, as can be seen in Figure 4.11.

FE measurements of the NWs produced revealed the enhanced electron emissive properties of the NWs, especially for CuO. Also a significant difference in the FE properties was observed, which can not be explained based on the macroscopic properties of the metal oxides. The work function of the oxide materials varied from 5 to 6 eV. This difference in work function value is not enough to explain the variation in the FE behavior. Therefore, the alteration in FE property should be explained by the NW morphology, i.e. by the shape of the individual NWs and their spatial density. The different metal oxide NWs observed in SEM and TEM have very similar quasi 1D shapes (either rod or needle-like structures). Therefore the enhancement factor and the field penetration effect for individual NWs should be similar. The main difference in the morphology, which can explain the difference in the FE efficiency, appeared to be the spatial density of NWs on the surface. It is interesting to note that ZnO and Fe_2O_3 NWs, which were synthesized with the highest NW density, showed the worst FE properties. In contrast, V_2O_5 and CuO NWs which demonstrated the highest FE efficiency were less uniform and had smaller NW density. As was reported previously [97], the highest current density corresponded to the optimum distance between emitters, which is a double emitter height. In other words, for the best electron emitting properties the distance between the NWs should be two times larger than their length. Therefore, in the case of ZnO and Fe_2O_3 NWs, the field enhancement factor for each emitter (NW) was significantly reduced due to the screening effect [97]. The difference in the emission site densities of different materials can be clearly seen in the FE patterns (Figure 4.11). Thus, the FE properties of the metal oxide NW samples are mainly determined by the spatial density of the NWs on the sample surface. It is worth noting that the efficient FE

from the metal oxide NWs examined is very promising for applications in vacuum electronic devices.

4.3.2 UV sensors

The UV-sensing phenomenon originates from the alteration of the charge carrier density. Under UV-light irradiation with a higher energy than the band gap of ZnO, the charge carrier density is increased, which reduces the resistance of the ZnO-Ts. When UV illumination is switched off, the oxygen chemisorption process dominates and assists photoconductivity relaxation [103].

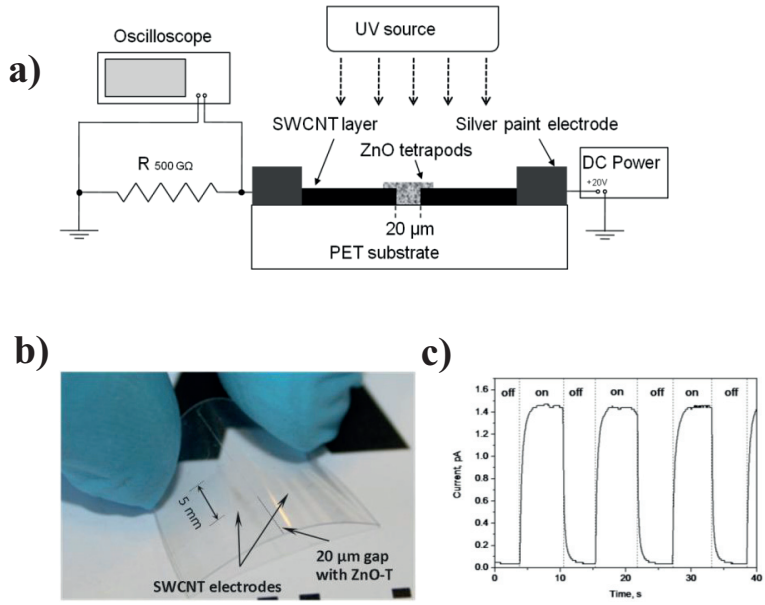

Figure 4.12. Zinc oxide tetrapods ultraviolet (UV) sensor: a) schematics of UV response measurement; b) a photo of the sensor; c) the sensor response to excitation at 365 nm.

The UV sensor response was measured using a digital oscilloscope (Tektronix DPO 2014) by a comparison method, where the magnitudes of a reference resistor and the UV sensor were compared by the voltage drop they inflicted on the circuit (Figure 4.12a). A constant potential (20 V) was applied over the UV sensor and a reference resistor (500 GΩ) connected in series. The voltage drop over the reference resistor was recorded in time while the UV illumination was turned on and off. Current flowing through the circuit was later resolved by applying Kirchhoff's law.

A flexible transparent UV sensor (Figure 4.12b) was made by drying a droplet of ZnO-T solution in ethanol between two transparent single-wall carbon nanotube (SWCNT) film contacts, on a polyethylene terephthalate (PET) substrate. SWCNT electrode fabrication is described in Refs [104,

105]; in short, a one-step process was used, whereby filtered SWCNTs without any post processing were transferred from a filter by pressing it onto a PET substrate. To obtain high optical transparency, sample synthesized at y_{Mg} = 2.3% and SWCNT electrodes with 95% transparency were used. UV sensing experiments were carried out under UV intensity of 30 μW/cm² at a wavelength of 365 nm. Fig. 8c shows the UV sensor response to the illumination. The initial current of 0.032 pA increased to 1.45 pA under the UV illumination, which is a 45 fold change. The response time to 90% of the current change was 0.9 s.

Our UV sensor configuration leads to potential barriers formed at the interfaces and junctions in the device (Figure 4.13), namely: i) SWCNT electrode and ZnO-T junction, ii) multiple ZnO-T leg to leg junctions, iii) interface between ZnO wurtzite legs and zinc blende core. The work function of the SWCNT electrode is 4.8 eV [106], and the electron affinity of ZnO is 4.5 eV [107], so a Schottky barrier between ZnO-Ts and SWCNTs is formed. Depletion layers at the ZnO-T leg surface induced by electron trapping form another multiple leg to leg potential barrier. The interface between the wurtzite legs and zinc blende core may also play a role in the transport mechanism as the contact barrier at the interface might lead to higher resistance; on the other hand, the volume of the zinc blende core can be negligibly small and make no considerable influence.

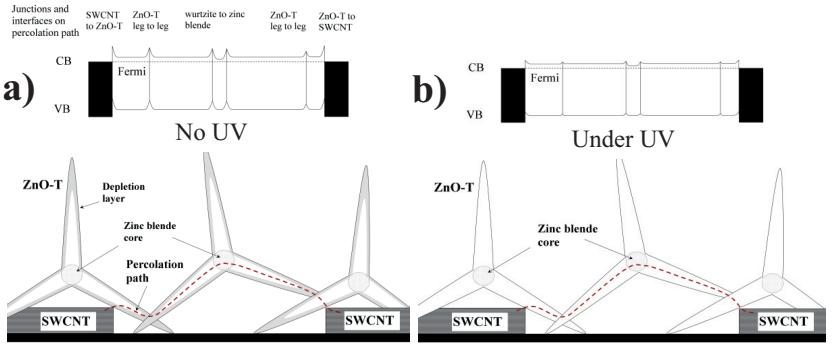

Figure 4.13. Schematics of barriers on zinc oxide tetrapods ultraviolet (UV) sensor percolation path: a) no UV illumination; b) under UV. CB and VB mean conduction and valance band, respectively.

The high performance of the device, comparing to single ZnO-T ohmic contact sensors [103, 108], is associated with the multiple barriers. The local electric field at the barrier area reduces the electron—hole recombination rates, resulting in an increase in free carrier density. Moreover, the UV-illumination-induced desorption of oxygen at the boundary changes the barrier height and narrows the barrier width, and

also improves UV sensitivity. Rapid photocurrent response and recovery is related to quick changes in the interfacial region, instead of the whole surface [109, 110]. It is also known that the higher the potential barrier, the faster the current recovery [111].

Response measurements show that such a photosensor is suitable for detection of low levels of UV light. Moreover the high resistance of 60 TΩ in the off state shows great potential for practical application in UV sensing.

6. Conclusions

A simple, rapid and inexpensive method for metal oxide NW growth based on the resistive heating of metals under ambient conditions was proposed and developed. As a result, Fe_2O_3, CuO, V_2O_5 and ZnO NWs were synthesized and thoroughly characterized. Fe_2O_3 NW formation was detected after only 2 s of heating; other metal oxide NWs were grown after 10 s. It was found that Fe_2O_3 NWs grew in the [110] crystallographic direction and contained stacking faults along the NW direction. The α-Fe_2O_3 NW growth rate under ambient conditions at 700 °C was found to exceed 100 nm/s.

The ZnO NW growth mechanism was investigated in the 400–850 °C temperature range . The highest ZnO NW growth rate was observed at 530 °C. It was found that the direction of the ZnO NW growth occurred along [110]. The growth rate showed parabolic dependence, which was explained by the Zn interstitial and vacancy migration. The ZnO NW growth activation energy E_a=83.8 kJ/mol, obtained from the Arrhenius plot, confirmed this result. The Zn interstitial and vacancy migration were deduced to be the limiting stage of the ZnO NWs growth.

The mechanism of metal oxide NW growth by oxidation is based on the diffusion of metal ions to the surface of the wire through grain boundaries and to the tip of the growing NW through defect diffusion and by surface diffusion. The growth mechanism was demonstrated for ZnO and Fe_2O_3 NWs, but it is also valid for the growth of other metal oxide NWs investigated in this work, namely CuO and V_2O_5.

Field emission from NWs, grown by the resistive heating method, exhibited promising results for applications in vacuum electronic devices. Cold electron FE measurements showed that CuO NWs have a very low threshold field of 4 V/μm at 0.01 mA/cm^2. The FE efficiency decrease for samples with a higher spatial density of NWs was explained by the screening effect.

A vertical flow reactor was designed and constructed for the controlled synthesis of ZnO-T structures. It was shown that the morphology of ZnO-Ts could be adjusted by Zn vapor pressure in the reactor by changing the evaporation temperature. The highest aspect ratio of ZnO-T legs was obtained at 700 °C and a Zn partial vapor pressure of 0.08 atm. Highly anisotropic structures were obtained because of the high Zn vapor pressure, favoring small nucleus diameters and fast kinetic growth. ZnO-Ts demonstrated the potential for application in transparent and flexible UV sensors and showed a 45-fold current increase under UV irradiation with an

intensity of 30 μW/cm² at a wavelength of 365 nm, and a response time of 0.9 s. The high performance of the device was explained by the multiple contact barriers.

7. References

1. Feynman, R., *There's Plenty of Room at the Bottom*. Engineering and Science, 1960. **23**(5): p. 22-36.
2. Takagi, R., *Growth of Oxide Whiskers on Metals at High Temperature*. Journal of the Physical Society of Japan, 1957. **12**(11): p. 1212-1218.
3. Wang, N., Y. Cai, and R.Q. Zhang, *Growth of nanowires*. Materials Science and Engineering: R: Reports, 2008. **60**(1-6): p. 1-51.
4. Lu, J.G., P. Chang, and Z. Fan, *Quasi-one-dimensional metal oxide materials—Synthesis, properties and applications*. Materials Science and Engineering: R: Reports, 2006. **52**(1-3): p. 49-91.
5. Wei, L. and M.L. Charles, *Semiconductor nanowires*. Journal of Physics D: Applied Physics, 2006. **39**(21): p. R387.
6. Takagi, H. and H.Y. Hwang, *An Emergent Change of Phase for Electronics*. Science, 2010. **327**(5973): p. 1601-1602.
7. Mannhart, J. and D.G. Schlom, *Oxide Interfaces-An Opportunity for Electronics*. Science, 2010. **327**(5973): p. 1607-1611.
8. Ohno, Y., *In-situ analysis of optoelectronic properties of twin boundaries in AlGaAs by polarized cathodoluminescence spectroscopy in a TEM*. Journal of Electron Microscopy, 2010. **59**(S1): p. S141-S147.
9. Nakamura, J. and A. Natori, - *Dielectric discontinuity at structural boundaries in Si*. Applied Physics Letters, 2006. **89**(5): p. 053118.
10. Zheng, G., et al., *Multiplexed electrical detection of cancer markers with nanowire sensor arrays*. Nat Biotech, 2005. **23**(10): p. 1294-1301.
11. Zhu, C.L., et al., *Synthesis and enhanced ethanol sensing properties of α-Fe2O3/ZnO heteronanostructures*. Sensors and Actuators B: Chemical, 2009. **140**(1): p. 185-189.
12. Zhu, Y.W. and et al., *Large-scale synthesis and field emission properties of vertically oriented CuO nanowire films*. Nanotechnology, 2005. **16**(1): p. 88.
13. Law, M., et al., *Nanowire dye-sensitized solar cells*. Nat Mater, 2005. **4**(6): p. 455-459.
14. Lin, Y., et al., *Nanonet-Based Hematite Heteronanostructures for Efficient Solar Water Splitting*. Journal of the American Chemical Society, 2011. **133**(8): p. 2398-2401.
15. Zhong Lin, W., *ZnO nanowire and nanobelt platform for nanotechnology*. Materials Science and Engineering: R: Reports, 2009. **64**(3-4): p. 33-71.
16. Yan, R., D. Gargas, and P. Yang, *Nanowire photonics*. Nat Photon, 2009. **3**(10): p. 569-576.
17. Yan, H., et al., *Programmable nanowire circuits for nanoprocessors*. Nature, 2011. **470**(7333): p. 240-244.
18. Li, Y., et al., *Nanowire electronic and optoelectronic devices*. Materials Today, 2006. **9**(10): p. 18-27.
19. Thelander, C., et al., *Nanowire-based one-dimensional electronics*. Materials Today, 2006. **9**(10): p. 28-35.
20. Calarco, R., et al., *Size-dependent Photoconductivity in MBE-Grown GaN–Nanowires*. Nano Letters, 2005. **5**(5): p. 981-984.
21. Chan, Y., et al., - *ZnSe nanowires epitaxially grown on GaP(111) substrates by molecular-beam epitaxy*. Applied Physics Letters, 2003. **83** (13): p. 2665-2667.

22. Park, D.J., et al., - *Defects in interfacial layers and their role in the growth of ZnO nanorods by metallorganic chemical vapor deposition*. Applied Physics Letters, 2007. **91**(14): p. 143115.
23. Yan, H., et al., *Morphogenesis of One-Dimensional ZnO Nano- and Microcrystals*. Advanced Materials, 2003. **15**(5): p. 402-405.
24. Chen, Z.-G., et al., *Synthesis and photoluminescence of tetrapod ZnO nanostructures*. Chemical Physics Letters, 2007. **434**(4-6): p. 301-305.
25. Dai, Z.R., Z.W. Pan, and Z.L. Wang, *Novel Nanostructures of Functional Oxides Synthesized by Thermal Evaporation*. Advanced Functional Materials, 2003. **13**(1): p. 9-24.
26. Polman, E.A., T. Fransen, and P.J. Gellings, *Oxidation kinetics of chromium and morphological phenomena*. Oxidation of Metals, 1989. **32**(5): p. 433-447.
27. Mikkelsen, L. and S. Linderoth, *High temperature oxidation of Fe–Cr alloy in O2–H2–H2O atmospheres; microstructure and kinetics*. Materials Science and Engineering: A, 2003. **361**(1-2): p. 198-212.
28. Wen, X., et al., *Controlled Growth of Large-Area, Uniform, Vertically Aligned Arrays of α-Fe2O3 Nanobelts and Nanowires*. The Journal of Physical Chemistry B, 2004. **109**(1): p. 215-220.
29. Jiang, X., T. Herricks, and Y. Xia, *CuO Nanowires Can Be Synthesized by Heating Copper Substrates in Air*. Nano Letters, 2002. **2**(12): p. 1333-1338.
30. Wu, Y., et al., *Growth of hexagonal tungsten trioxide tubes*. Journal of Crystal Growth, 2006. **292**(1): p. 143-148.
31. Mozetič, M., et al., *A Method for the Rapid Synthesis of Large Quantities of Metal Oxide Nanowires at Low Temperatures*. Advanced Materials, 2005. **17**(17): p. 2138-2142.
32. Husnu Emrah, U. and et al., *Rapid synthesis of aligned zinc oxide nanowires*. Nanotechnology, 2008. **19**(25): p. 255608.
33. Guo, M., P. Diao, and S. Cai, *Hydrothermal growth of well-aligned ZnO nanorod arrays: Dependence of morphology and alignment ordering upon preparing conditions*. Journal of Solid State Chemistry, 2005. **178**(6): p. 1864-1873.
34. Zhang, J., et al., *A simple method to synthesize β-Ga2O3 nanorods and their photoluminescence properties*. Journal of Crystal Growth, 2005. **280**(1-2): p. 99-106.
35. Murphy, C.J., et al., *Anisotropic Metal Nanoparticles: Synthesis, Assembly, and Optical Applications*. The Journal of Physical Chemistry B, 2005. **109**(29): p. 13857-13870.
36. Jun, Y.-w., J.-s. Choi, and J. Cheon, *Shape Control of Semiconductor and Metal Oxide Nanocrystals through Nonhydrolytic Colloidal Routes*. Angewandte Chemie International Edition, 2006. **45**(21): p. 3414-3439.
37. Vantomme, A., et al., *Surfactant-Assisted Large-Scale Preparation of Crystalline CeO2 Nanorods*. Langmuir, 2004. **21**(3): p. 1132-1135.
38. Mintz, T.S., et al., *Electrochemical Synthesis of Functionalized Nickel Oxide Nanowires*. Electrochemical and Solid-State Letters, 2005. **8**(9): p. D26-D30.
39. Wagner, R. and W. Ellis, - *Vapor-Liquid-Solid Mechanism of Single Crystal Growth*. Applied Physics Letters, 1964. **4**(5): p. 89-90.
40. Liu, X., et al., - *Growth mechanism and properties of ZnO nanorods synthesized by plasma-enhanced chemical vapor deposition*. Journal of Applied Physics, 2004. **95**(6): p. 3141 - 3147.
41. Kodambaka, S., et al., *Germanium Nanowire Growth Below the Eutectic Temperature*. Science, 2007. **316**(5825): p. 729-732.

42. Persson, A.I., et al., *Solid-phase diffusion mechanism for GaAs nanowire growth*. Nat Mater, 2004. **3**(10): p. 677-681.
43. Wen, C.-Y., et al., *Formation of Compositionally Abrupt Axial Heterojunctions in Silicon-Germanium Nanowires*. Science, 2009. **326**(5957): p. 1247-1250.
44. Gamalski, A.D., et al., *Formation of Metastable Liquid Catalyst during Subeutectic Growth of Germanium Nanowires*. Nano Letters, 2010. **10**(8): p. 2972-2976.
45. Hofmann, S., et al., *Ledge-flow-controlled catalyst interface dynamics during Si nanowire growth*. Nat Mater, 2008. **7**(5): p. 372-375.
46. Dick, K.A., et al., *A New Understanding of Au-Assisted Growth of III–V Semiconductor Nanowires*. Advanced Functional Materials, 2005. **15**(10): p. 1603-1610.
47. Gamalski, A.D., C. Ducati, and S. Hofmann, *Cyclic Supersaturation and Triple Phase Boundary Dynamics in Germanium Nanowire Growth*. The Journal of Physical Chemistry C, 2011. **115**(11): p. 4413-4417.
48. Stach, E.A., et al., *Watching GaN Nanowires Grow*. Nano Letters, 2003. **3**(6): p. 867-869.
49. Mattila, M., T. Hakkarainen, and H. Lipsanen, *Catalyst-free fabrication of InP and InP(N) nanowires by metalorganic vapor phase epitaxy*. Journal of Crystal Growth, 2007. **298**(0): p. 640-643.
50. Oh, S.H., et al., *Oscillatory Mass Transport in Vapor-Liquid-Solid Growth of Sapphire Nanowires*. Science, 2010. **330**(6003): p. 489-493.
51. Novotny, C.J., *Vertically aligned, catalyst-free InP nanowires grown by metalorganic chemical vapor deposition*. Appl. Phys. Lett., 2005. **87**(20): p. 203111.
52. Wohlfart, A., et al., *Morphology controlled growth of arrays of GaN nanopillars and randomly distributed GaN nanowires on sapphire using $(N_3)_2Ga[(CH_2)_3NMe_2]$ as a single molecule precursor*. Chemical Communications, 2002(9): p. 998-999.
53. Parala, H., et al., *Investigations on InN whiskers grown by chemical vapour deposition*. Journal of Crystal Growth, 2001. **231**(1-2): p. 68-74.
54. Frank, F.C., *The influence of dislocations on crystal growth*. Discussions of the Faraday Society, 1949. **5**: p. 48-54.
55. Burton, W.K., N. Cabrera, and F.C. Frank, *Role of Dislocations in Crystal Growth*. Nature, 1949. **163**(4141): p. 398-399.
56. Burton, W.K., N. Cabrera, and F.C. Frank, *The Growth of Crystals and the Equilibrium Structure of their Surfaces*. Philosophical Transactions of the Royal Society of London. Series A, Mathematical and Physical Sciences, 1951. **243**(866): p. 299-358.
57. Sears, G.W., *Mercury Whiskers*. Acta Metallurgica, 1953. **1**(4): p. 457-459.
58. Sears, G.W., *A growth mechanism for mercury whiskers*. Acta Metallurgica, 1955. **3**(4): p. 361-366.
59. Bierman, M.J., et al., *Dislocation-Driven Nanowire Growth and Eshelby Twist*. Science, 2008. **320**(5879): p. 1060-1063.
60. Morin, S.A., et al., *Mechanism and Kinetics of Spontaneous Nanotube Growth Driven by Screw Dislocations*. Science, 2010. **328**(5977): p. 476-480.
61. de Faria, D.L.A., S. Venâncio Silva, and M.T. de Oliveira, *Raman microspectroscopy of some iron oxides and oxyhydroxides*. Journal of Raman Spectroscopy, 1997. **28**(11): p. 873-878.

62. de Faria, D.L.A. and F.N. Lopes, *Heated goethite and natural hematite: Can Raman spectroscopy be used to differentiate them?* Vibrational Spectroscopy, 2007. **45**(2): p. 117-121.
63. Chrzanowski, J. and J.C. Irwin, *Raman scattering from cupric oxide*. Solid State Communications, 1989. **70**(1): p. 11-14.
64. Pérez-Robles, F., et al., *Raman study of copper and iron oxide particles embedded in an SiO2 matrix*. Journal of Raman Spectroscopy, 1999. **30**(12): p. 1099-1104.
65. Petroff, Y., P.Y. Yu, and Y.R. Shen, *Study of photoluminescence in Cu_2O*. Physical Review B, 1975. **12**(6): p. 2488.
66. Compaan, A. and H.Z. Cummins, *Raman Scattering, Luminescence, and Exciton-Phonon Coupling in Cu_2O*. Physical Review B, 1972. **6**(12): p. 4753.
67. Reimann, K. and K. Syassen, *Raman scattering and photoluminescence in Cu_2O under hydrostatic pressure*. Physical Review B, 1989. **39**(15): p. 11113.
68. Mayer, S.T. and R.H. Muller, *An In Situ Raman Spectroscopy Study of the Anodic Oxidation of Copper in Alkaline Media*. Journal of The Electrochemical Society, 1992. **139**(2): p. 426-434.
69. Chou, M.H., et al., *Confocal Raman spectroscopic mapping studies on a single CuO nanowire*. Applied Surface Science, 2008. **254**(23): p. 7539-7543.
70. Shin, D.H., et al., *Preparation of vanadium pentoxide powders by microwave plasma-torch at atmospheric pressure*. Materials Chemistry and Physics, 2006. **99**(2-3): p. 269-275.
71. Ramana, C.V., et al., *Surface analysis of pulsed laser-deposited V2O5 thin films and their lithium intercalated products studied by Raman spectroscopy*. Surface and Interface Analysis, 2005. **37**(4): p. 406-411.
72. Su, Q., et al., *Formation of vanadium oxides with various morphologies by chemical vapor deposition*. Journal of Alloys and Compounds, 2009. **475**(1-2): p. 518-523.
73. Pan, M., et al., *Raman study of the phase transition in VO_2 thin films*. Journal of Crystal Growth, 2004. **268**(1-2): p. 178-183.
74. Manning, T.D. and I.P. Parkin, *Vanadium(IV) oxide thin films on glass and silicon from the atmospheric pressure chemical vapour deposition reaction of $VOCl_3$ and water*. Polyhedron, 2004. **23**(18): p. 3087-3095.
75. Wang, X., *Low-temperature growth and properties of ZnO nanowires*. Appl. Phys. Lett., 2004. **84**(24): p. 4941.
76. Pan, H., et al., *Optical and Field Emission Properties of Zinc Oxide Nanostructures*. Journal of Nanoscience and Nanotechnology, 2005. **5**(10): p. 1683-1687.
77. Bocquet, A.E., et al., *Electronic structure of 3d-transition-metal compounds by analysis of the 2p core-level photoemission spectra*. Physical Review B, 1992. **46**(7): p. 3771.
78. Aronniemi, M., J. Sainio, and J. Lahtinen, *Chemical state quantification of iron and chromium oxides using XPS: the effect of the background subtraction method*. Surface Science, 2005. **578**(1-3): p. 108-123.
79. Moulder, J.F., *Handbook of X-ray Photoelectron Spectroscopy: A Reference Book of Standard Spectra for Identification and Interpretation of XPS Data*. 1992: Eden Prairie, MN: Perkin-Elmer.
80. Silversmit, G., et al., *Determination of the V2p XPS binding energies for different vanadium oxidation states (V^{5+} to V^{0+})*. Journal of Electron Spectroscopy and Related Phenomena, 2004. **135**(2-3): p. 167-175.

81. Geguzin, I.E., *The diffusion zone*. 1979, Nauka: Moscow. p. 344.
82. Young, D., *High temperature oxidation and corrosion of metals*. 2008, Elsevier. p. 592.
83. Smeltzer, W.W. and D.J. Young, *Oxidation properties of transition metals*. Progress in Solid - State Chemistry, 1975. **10**: p. 17-54.
84. Tomlins, G.W., J.L. Routbort, and T.O. Mason, *Zinc self-diffusion, electrical properties, and defect structure of undoped, single crystal zinc oxide*. Journal of Applied Physics, 2000. **87**(1): p. 117-123.
85. Wagner, C., *Equations for transport in solid oxides and sulfides of transition metals*. Progress in Solid - State Chemistry, 1975. **10**(1): p. 14.
86. Khristoforov, K.K., et al., *Kinetics of grain growth in a zinc oxide ceramic*. Glass and Ceramics, 1986. **43**(4): p. 171-173.
87. Young, D., *High Temperature Oxidation and Corrosion of Metals*. Elsevier Corrosion Series. 2008, Oxford.
88. Voss, D., E. Butler, and T. Mitchell, *The Growth of Hematite Blades during the High Temperature Oxidation of Iron*. Metallurgical and Materials Transactions A, 1982. **13**(5): p. 929-935.
89. Raynaud, G.M. and R.A. Rapp, *<i>In situ</i> observation of whiskers, pyramids and pits during the high-temperature oxidation of metals*. Oxidation of Metals, 1984. **21**(1): p. 89-102.
90. Hiralal, P. and et al., *Growth and process conditions of aligned and patternable films of iron(III) oxide nanowires by thermal oxidation of iron*. Nanotechnology, 2008. **19**(45): p. 455608.
91. Newton, M.C. and P.A. Warburton, *ZnO tetrapod nanocrystals*. Materials Today, 2007. **10**(5): p. 50-54.
92. Yin, Y. and A.P. Alivisatos, *Colloidal nanocrystal synthesis and the organic-inorganic interface*. Nature, 2005. **437**(7059): p. 664-670.
93. Ding, Y., et al., *Zinc-blende ZnO and its role in nucleating wurtzite tetrapods and twinned nanowires*. Applied Physics Letters, 2007. **90**(15): p. 153510.
94. Watt, J., et al., *Synthesis and Structural Characterization of Branched Palladium Nanostructures*. Advanced Materials, 2009. **21**(22): p. 2288.
95. Penn, R.L., *Kinetics of oriented aggregation*. Journal of Physical Chemistry B, 2004. **108**(34): p. 12707-12712.
96. Cozzoli, P.D., et al., *ZnO nanocrystals by a non-hydrolytic route: Synthesis and characterization*. Journal of Physical Chemistry B, 2003. **107**(20): p. 4756-4762.
97. Kleshch, V.I., A.N. Obraztsov, and E.D. Obraztsova, *Modeling of Field Emission from Nano Carbons*. Fullerenes, Nanotubes and Carbon Nanostructures, 2008. **16**(5-6): p. 384-388.
98. Gomer, R., *Field Emission and Field Ionization*. 1993, New York: AIP.
99. Shang, D., et al., *Magnetic and field emission properties of straw-like CuO nanostructures*. Applied Surface Science, 2009. **255**(7): p. 4093-4096.
100. Chen, W., et al., *Field Emission from V2O5.nH2O Nanorod Arrays*. The Journal of Physical Chemistry C, 2008. **112**(7): p. 2262-2265.
101. Barclay, P., *Probing the dispersive and spatial properties of photonic crystal waveguides via highly efficient coupling from fiber tapers*. Appl. Phys. Lett., 2004. **85**(1): p. 4.
102. Lee, W., et al., *Field emission characteristics of ZnO nanoneedle array cell under ultraviolet irradiation*. Physics Letters A, 2007. **370**(3-4): p. 345-350.
103. Lupan, O., L. Chow, and G.Y. Chai, *A single ZnO tetrapod-based sensor*. Sensors and Actuators B-Chemical, 2009. **141**(2): p. 511-517.

104. Nasibulin, A.G., et al., *Multifunctional Free-Standing Single-Walled Carbon Nanotube Films*. ACS Nano, 2011 **5**(4): p. 3214-3221.
105. Kaskela, A., et al., *Aerosol-Synthesized SWCNT Networks with Tunable Conductivity and Transparency by a Dry Transfer Technique*. Nano Letters, 2010. **10**(11): p. 4349-4355.
106. Suzuki, S., et al., *Work functions and valence band states of pristine and Cs-intercalated single-walled carbon nanotube bundles*. Vol. 76. 2000: AIP. 4007-4009.
107. Song, J., J. Zhou, and Z.L. Wang, *Piezoelectric and Semiconducting Coupled Power Generating Process of a Single ZnO Belt/Wire. A Technology for Harvesting Electricity from the Environment*. Nano Letters, 2006. **6**(8): p. 1656-1662.
108. Lupan, O., et al., *Focused-ion-beam fabrication of ZnO nanorod-based UV photodetector using the in-situ lift-out technique*. Physica Status Solidi a-Applications and Materials Science, 2008. **205**(11): p. 2673-2678.
109. Hu, Y., et al., *Supersensitive, Fast-Response Nanowire Sensors by Using Schottky Contacts*. Advanced Materials, 2010. **22**(30): p. 3327-3332.
110. Zhou, J., et al., *Gigantic enhancement in response and reset time of ZnO UV nanosensor by utilizing Schottky contact and surface functionalization*. Applied Physics Letters, 2009. **94**(19): p. 191103.
111. Yanbo, L. and et al., *Bascule nanobridges self-assembled with ZnO nanowires as double Schottky barrier UV switches*. Nanotechnology, 2010. **21**(29): p. 295502.

Nanowires (NWs), exhibit extraordinary properties, distinctive from the bulk material, and therefore are an excellent material for nanoscale applications. The vast majority of methods for NW fabrication use catalysts, however, catalyst-free methods offer the facile fabrication of pure nanowires with fewer technological steps. For the development of non-catalytic techniques an understanding of the growth mechanism is crucial. The aim of this thesis was to propose and to develop novel techniques for the non-catalytic synthesis of metal oxide NWs, to examine their structures and properties, and to investigate their growth mechanisms and potential applications. Two different approaches were applied for the synthesis: metal resistive heating and vapor growth methods. The NW growth mechanism during the metal oxidation was studied. The vapor growth method was utilized for the synthesis of ZnO tetrapods. The synthesized NWs were examined for field emission (FE) and ultraviolet (UV) sensing applications.

ISBN 978-952-60-4405-7
ISBN 978-952-60-4406-4 (pdf)
ISSN-L 1799-4934
ISSN 1799-4934
ISSN 1799-4942 (pdf)

Aalto University
School of Science
Department of Applied Physics
www.aalto.fi

BUSINESS + ECONOMY

ART + DESIGN + ARCHITECTURE

SCIENCE + TECHNOLOGY

CROSSOVER

DOCTORAL DISSERTATIONS

Aalto-DD 132/2011

Simas Rackauskas

Non-catalytic growth of metal oxide nanowires: properties and growth mechanism investigations

Aalto University